

1 **Reliability of Matching AMPERE Field-Aligned**
2 **Current Boundaries with SuperDARN Lower Latitude**
3 **Ionospheric Convection Boundaries During**
4 **Geomagnetic Storms**

5 **M.-T. Walach¹, A. R. Fogg², J. C. Coxon³, A. Grocott¹, S. E. Milan⁴, H. K.**
6 **Sangha⁵, K. A. McWilliams⁶, S. K. Vines⁷, M. Lester⁴, B. J. Anderson⁸**

7 ¹Lancaster University, Physics Department, Bailrigg, Lancaster, LA1 4YW, UK.

8 ²School of Cosmic Physics, DIAS Dunsink Observatory, Dublin Institute for Advanced Studies, Dublin 15,
9 Ireland.

10 ³Department of Mathematics, Physics and Electrical Engineering, Northumbria University, Newcastle
11 Upon Tyne, UK.

12 ⁴University of Leicester, Department of Physics and Astronomy, Leicester, UK.

13 ⁵UK Space Agency, Harwell, OX11 0FD, UK.

14 ⁶University of Saskatchewan, Saskatchewan, Canada.

15 ⁷Southwest Research Institute, San Antonio, TX, USA.

16 ⁸Johns Hopkins University Applied Physics Laboratory, Laurel, MD, USA.

17 **Key Points:**

- 18 • When SuperDARN data coverage is good, agreement can be found between the
19 Heppner-Maynard boundary and the field-aligned current boundary.
20 • The Heppner-Maynard boundary often lies 3° equatorward of the field-aligned cur-
21 rent boundary.
22 • Poor agreement tends to stem from poor data coverage or asymmetries in the field-
23 aligned currents.

Corresponding author: Maria-Theresia Walach, m.walach@lancaster.ac.uk

Abstract

High-latitude ionospheric convection is a useful diagnostic of solar wind-magnetosphere interactions and nightside activity in the magnetotail. For decades, the high-latitude convection pattern has been mapped using the Super Dual Auroral Radar Network (SuperDARN), a distribution of ground-based radars which are capable of measuring line-of-sight (l-o-s) ionospheric flows. From the l-o-s measurements an estimate of the global convection can be obtained. As the SuperDARN coverage is not truly global, it is necessary to constrain the maps when the map fitting is performed. The lower latitude boundary of the convection, known as the Heppner-Maynard boundary (HMB), provides one such constraint. In the standard SuperDARN fitting, the HMB location is determined directly from the data, but data gaps can make this challenging. In this study we evaluate if the HMB placement can be improved using data from the Active Magnetosphere and Planetary Electrodynamics Response Experiment (AMPERE), in particular for active time periods when the HMB moves to latitudes below 55° . We find that the boundary as defined by SuperDARN and AMPERE are not always co-located. SuperDARN performs better when the AMPERE currents are very weak (e.g. during non-active times) and AMPERE can provide a boundary when there is no SuperDARN scatter. Using three geomagnetic storm events, we show that there is agreement between the SuperDARN and AMPERE boundaries but the SuperDARN-derived convection boundary mostly lies $\sim 3^\circ$ equatorward of the AMPERE-derived boundary. We find that disagreements primarily arise due to geometrical factors and a time lag in expansions and contractions of the patterns.

Plain Language Summary

The high-latitude ionosphere, a part of Earth's upper atmosphere filled with ions and electrons, moves in response to solar wind and other space weather activities. This movement, known as ionospheric convection, is key to understanding how magnetic fields and plasma interact in space. To study this, scientists use the Super Dual Auroral Radar Network (SuperDARN), a ground-based system designed to measure these ionospheric movements. For years, researchers have questioned whether the methods used to combine SuperDARN data into convection maps are the best they can be. A crucial part of this process is determining the point at lower latitudes, where convection slows down. This can be done using SuperDARN data or data from spacecraft. For example, data from the Active Magnetosphere and Planetary Electrodynamics Response Experiment (AMPERE) from the Iridium satellites can be used for this. AMPERE provides a measure of the electric currents that are associated with the convection. We compare two methods with ground-based radars and spacecraft, to see if the boundaries match. The main finding is that they often do not, with the spacecraft and radar data showing different convection boundaries. This disagreement challenges our understanding of plasma physics, as both methods should ideally show similar results.

1 Introduction

Plasma circulates in the terrestrial magnetosphere due to the Dungey cycle, whereby reconnection on the dayside of the magnetosphere opens magnetic flux and nightside reconnection in the magnetotail closes magnetic flux (Dungey, 1961, 1963). Since ionospheric plasma can be largely said to be frozen-in (i.e. it circulates with the magnetic flux), the ionosphere also follows this circulation pattern. This is known as 'convection'. On average, the reconnection-driven plasma flows generate a dual-cell convection pattern in the ionosphere (e.g. Obayashi & Nishida, 1968; Heppner, 1972; Stern, 1977; Heppner & Maynard, 1987, and references within). Plasma flows from the dayside to the nightside across the pole and returns via the dusk and dawn sides at lower latitudes. Ionospheric convection is a key indicator of the state of the magnetosphere. Due to the solar wind-

74 magnetosphere-ionosphere coupling, the plasma convection in the ionosphere changes in
 75 response to changes in the solar wind driving and magnetospheric response (as explic-
 76 itly shown by Walach et al., 2017a). The ionosphere also responds to changes in the mag-
 77 netosphere, which may not be in direct response to solar wind drivers. Substorms, which
 78 result from reconnection in the magnetotail, are at times an example of this. Substorms
 79 can accelerate plasma flows in the ionosphere and change the geometry of convection (Heppner,
 80 1972; Provan et al., 2004; Bristow & Jensen, 2007a).

81 Electric currents flow due to deformations in the Earth’s magnetic fields, which make
 82 it non-dipolar (Parker, 1996, 1997; Vasyliunas, 2001, 2005; Milan et al., 2017). Within
 83 the magnetosphere, currents are thought to connect the ionosphere to the magnetopause
 84 and the ring current (Iijima & Potemra, 1978). These are known as Birkeland currents
 85 (Birkeland, 1908, 1913) or field-aligned currents (FACs). In the ionosphere, they can be
 86 split into two interlaced systems: the region 1 (R1) and region 2 (R2) currents, which
 87 are connected through the conducting ionosphere. The R1 currents form a rough oval
 88 around the magnetic pole with current flowing away from the ionosphere on the dusk
 89 side and current flowing into the ionosphere on the dawn side. The R2 currents flow at
 90 a lower latitude than the R1 currents and also form a roughly concentric ring. The R2
 91 currents flow in opposite directions up and down the field lines to their neighbouring R1
 92 currents and form a pair of semi-circles (e.g. Coxon et al., 2014, 2018). The locations
 93 where the FACs flow into and out of the ionosphere can be described in terms of con-
 94 vection vorticity and hence, when we assume a uniform conductivity, they must match
 95 where the plasma flows change direction theoretically (Sofko et al., 1995). The R1 cur-
 96 rents are also co-located with the boundary between the open and closed field lines (Lockwood,
 97 1991; Cowley & Lockwood, 1992; Clausen et al., 2013; Milan et al., 2017), but whilst the
 98 R1 currents provide a fuzzy boundary, the boundary between open and closed field lines
 99 is discrete.

100 FACs can also be present in the magnetosphere due to field line resonances, and
 101 these can generate auroras (e.g. Milan et al., 2001; Rankin et al., 2005). Using magne-
 102 tohydrodynamic (MHD) wave coupling and phase mixing in a model of the magneto-
 103 sphere, FACs currents which resemble the R1 and R2 systems can be modelled (e.g. Wright
 104 & Elsden, 2020; Elsden et al., 2022). This MHD modelling shows that during geomag-
 105 netic storms, the FACs and field line resonances which are located outside the plasma-
 106 sphere, move closer to the Earth (Elsden et al., 2022).

107 Furthermore, the aurora is expected to be colocated with the FACs (Carter et al.,
 108 2016). For example, McWilliams et al. (2001) used Super Dual Auroral Radar Network
 109 (SuperDARN) measurements of ionospheric plasma vorticity to estimate the FAC per
 110 unit Pedersen conductance and found that the upward FACs were colocated with au-
 111 roral emission from the Polar Visible Imaging System (VIS) in the post-noon sector.

112 Theoretically, the equatorward edge of the locations where R2 currents flow should
 113 match with the equatorial convection boundary (e.g. Milan et al., 2017, and references
 114 therein). Using FACs inferred from ground magnetometers, Weygand et al. (2023) cor-
 115 related the magnetic latitudes of these equatorward boundaries with a variety of param-
 116 eters and showed that the highest correlation is found with IMF B_Z . Further, Weygand
 117 et al. (2023) showed that the next most important correlations of the equatorward bound-
 118 ary latitude are found to be with the SYM-H index and the mean solar wind electric field
 119 with respect to the reference frame of earth (VB_Z). Their study also showed that dur-
 120 ing storms, the equatorward boundary extends to 45° magnetic latitude.

121 Data from SuperDARN coherent ionospheric scatter radars can be used to build
 122 large-scale maps of ionospheric convection and they provide a rich dataset, having been
 123 running since the 1990s (Greenwald et al., 1995; Chisham et al., 2007; Lester, 2008; Nishi-
 124 tani et al., 2019). The radars are able to measure line-of-sight ionospheric velocities and
 125 we combine the data to make convection maps following the procedure initially outlined

126 by Ruohoniemi and Baker (1998), and often termed the “map potential technique”. One
 127 step in this process, discussed in detail by Shepherd and Ruohoniemi (2000), is to fit a
 128 lower-latitude boundary to the convection, which is known as the Heppner-Maynard Bound-
 129 ary (HMB). In the SuperDARN fitting process, the HMB has a form which is circular
 130 on the nightside and tapers off to higher latitudes on the dayside. Shepherd and Ru-
 131 ohoniemi (2000) chose this form after a statistical study by Heppner and Maynard (1987)
 132 who found that the ovoid shape on the dayside together with the circular shape on the
 133 nightside is a better fit for the HMB than a simple circle. In the standard SuperDARN
 134 fitting technique, the HMB is chosen at 1° below the lowest latitude where at least three
 135 SuperDARN flow vectors reach above 100 m/s (SuperDARN Data Analysis Working Group,
 136 Thomas, Ponomarenko, Bland, et al., 2018). However, this can lead to inconsistencies,
 137 since SuperDARN backscatter is not always present everywhere due technical, as well
 138 as, geophysical reasons. This technique is conventionally used when making convection
 139 maps and is what we use in this study. See section 2 for further details of the SuperDARN
 140 fitting algorithm.

141 The HMB sits at the lower latitude of the convection cells, where the electric field
 142 theoretically goes to zero. Imber et al. (2013a) studied the HMB measured by Super-
 143 DARN and found that, on average, it lies just a few degrees equatorward of the latitude
 144 where the auroral oval is brightest. In their study, Imber et al. (2013a) considered data
 145 from 2000-2002 where SuperDARN data was available at the same time as auroral data
 146 as from the Imager for Magnetopause-to-Aurora Global Exploration (IMAGE) satellite,
 147 which allowed for a systematic study of the two boundaries. The results showed that the
 148 two are often systematically offset. The average measured offset was 2.2° , with the au-
 149 roral latitude lying $0-3^\circ$ poleward of the HMB during $\sim 55\%$ of the 2 min intervals. Imber
 150 et al. (2013a) also noted that larger offsets often correspond to substorm or geomagnetic
 151 storm times. It is worth noting that for the time period of data analysed by Imber et
 152 al. (2013a), no mid-latitude data was available. As was shown by Walach et al. (2021)
 153 mid-latitude radar data are important when choosing the HMB.

154 Fogg et al. (2020) used FAC data from the Active Magnetosphere and Planetary
 155 Electrodynamics Response Experiment (AMPERE, Anderson et al., 2000, 2014; Wa-
 156 ters et al., 2001; Coxon et al., 2018) to show that there is a statistical relationship be-
 157 tween the boundary between R1 and R2 and the HMB. The relationship from Fogg et
 158 al. (2020) was developed as an alternative for the HMB used for the SuperDARN fitting
 159 algorithm. Fogg et al. (2020) used data from the solar minimum and maximum (2011
 160 and 2015, respectively) to match the R1/R2 FAC location to the SuperDARN HMB. This
 161 yielded a linear relationship, which can be used as an input into the SuperDARN fitting,
 162 when AMPERE R1/R2 boundaries are available. Walach and Grocott (2019) and Walach
 163 et al. (2021) found however that during geomagnetic storms, the HMB moves to lower
 164 latitudes than previously thought. Similarly, Coxon et al. (2017) showed that the R2 cur-
 165 rent intensifies during substorms, which implies that the HMB is also lowered during sub-
 166 storms as was indeed shown by Bristow and Jensen (2007b) using SuperDARN data. Whilst
 167 Coxon et al. (2023) showed that the most intense currents measured by AMPERE were
 168 found on the dayside, the currents shown in their study also expanded to lower latitudes
 169 during geomagnetic storms. Walach and Grocott (2019) found that the convection can
 170 expand to as low as 40° magnetic latitude during geomagnetic storms as measured by
 171 SuperDARN, which is the current observational SuperDARN limit. Conversely to the
 172 45° limit found by Weygand et al. (2023), the saturation of data points at the observa-
 173 tional limit found by Walach and Grocott (2019) suggests that the equatorward bound-
 174 ary of the convection is likely to reach even lower than 40° magnetic latitude. Similar
 175 to Weygand et al. (2023), Walach et al. (2022a) also showed that the HMB moves to lower
 176 latitudes with increased SYM-H. However, the relationship breaks down for extremely
 177 negative values of SYM-H, which is likely due to the observational limit of the mid-latitude
 178 radars constraining the HMB. Prior to mid-latitude SuperDARN data being available
 179 (e.g. data analysed by Imber et al., 2013b, 2013a), the HMB limit was located at 50°

180 latitude, which would have misplaced $\sim 19\%$ of the HMBs during geomagnetic storms
 181 (Walach & Grocott, 2019).

182 Since the data from Fogg et al. (2020) did not explicitly include any geomagnetic
 183 storms, the question remains: Is the field aligned current-derived boundary location a
 184 good proxy for the SuperDARN ionospheric convection boundary during storms? If the
 185 data from Fogg et al. (2020) can be extrapolated linearly, we may expect the answer to
 186 be a simple ‘yes’, but Walach et al. (2022a) showed that the HMB behaves non-linearly
 187 with increasing geomagnetic activity. If field-aligned current is not always a good proxy,
 188 what controls this? We expect the magnetosphere to behave differently during geomag-
 189 netic storms. The ring current, for example, is enhanced and the inner magnetosphere
 190 changes, which affects the boundary between the convecting and non-convecting plasma
 191 (i.e. the plasmopause) (Gonzalez et al., 1994; Wharton et al., 2020; Sandhu, Rae, & Walach,
 192 2021; Sandhu, Rae, Wygant, et al., 2021; Sandhu, Rae, Staples, et al., 2021; Pierrard et
 193 al., 2021; Elsdén et al., 2022).

194 Where the HMB or convection boundary is truly located and how this relates to
 195 the R1 and R2 currents is further complicated by time-varying phenomena. For exam-
 196 ple, Sangha et al. (2020) showed that the R2 FACs can bifurcate into two channels and
 197 the lower latitude branch can split off. Sangha et al. (2020) relates the later stages of
 198 bifurcations with evidence for Subauroral polarization streams (SAPS). SAPS create large
 199 plasma flows and electric fields in the sub-auroral ionosphere and are thus of interest to
 200 Space Weather. Sangha et al. (2020) showed that bifurcations commonly lead to SAPS
 201 and are more likely to occur during substorms. The bifurcations originate in the R2 FACs,
 202 and hence these bifurcations are tied to the convection pattern at some point prior to
 203 connecting to a SAPS. Understanding when they separate from the R2 region and at what
 204 point they become an ionospheric plasma flow phenomenon which is latitudinally sep-
 205 arate from the dual-cell convection is important to understanding the relationship be-
 206 tween the HMB and the FAC systems, and thus the coupled magnetosphere and iono-
 207 sphere.

208 In this study, we compare the FAC location to the SuperDARN convection maps
 209 during some case studies to determine if the linear relationship found by Fogg et al. (2020)
 210 can be extrapolated to include more active times, such as geomagnetic storms. We have
 211 identified three events in which the HMB moves to low latitudes ($\sim 40^\circ$). As such, the
 212 Fogg et al. (2020) algorithm was not trained on this data and we can see how it performs
 213 against the SuperDARN maps. The solar wind driving and resulting geomagnetic condi-
 214 tions are shown in Figures S1 to S3 in the Supporting Information. These show that
 215 we study a variety of conditions leading to geomagnetic storms of varying strength with
 216 the first one being the weakest storm and the last one being the strongest. In section 2
 217 we describe the data used in this study, in section 3 we present data in the format of three
 218 case studies and in section 4 we discuss these results.

219 **2 Data**

220 **2.1 SuperDARN**

221 SuperDARN is a network of coherent radars which were built to remotely sense con-
 222 vection in the ionosphere. Their line of sight convection measurements can be combined
 223 to make convection maps. These SuperDARN convection maps provide a quantitative
 224 representation of the convection field in the high-latitude ionosphere. This is achieved
 225 by fitting spherical harmonic functions to line-of-sight velocities collected by the radars
 226 (e.g. Chisham et al., 2007; Nishitani et al., 2019). Different methods for fitting the con-
 227 vection maps exist and in this study we use a standard method introduced and bench-
 228 marked against other techniques by Walach et al. (2022a). In Walach et al. (2022a) five
 229 datasets were studied (D0-D4) and we use the final dataset D4 in this study. The D4

dataset includes all radars in the Northern Hemisphere and was processed using the Radar Software Toolkit v4.2 (SuperDARN Data Analysis Working Group, Thomas, Ponomarenko, Billett, et al., 2018) with the Thomas and Shepherd (2018) background model. For more information on how this dataset was processed and compares to older convection maps, measured parameters and dusk-dawn asymmetries, we refer the reader to Walach et al. (2022a, 2022b). This convection map dataset is simply referred to as the SuperDARN data in what follows and all vectors shown are the velocities from the spherical harmonic fitting procedure (Ruohoniemi & Baker, 1998).

The most important processing step for this study is how we choose the HMB. We will refer to the SuperDARN HMB as Λ_{Walach} throughout this study. This was fitted using the SuperDARN processing technique whereby the algorithm uses the data to find the HMB. The algorithm places the HMB at 1° below the lowest latitude where a minimum number of backscatter echoes are above a certain velocity threshold. In the SuperDARN processing, these values can be adjusted. We use a threshold of 100 m/s and the minimum number of vectors which has to be above this minimum magnitude is three, a commonly used combination (e.g., Walach et al., 2022a), and the same criterion as originally defined by Shepherd and Ruohoniemi (2000).

2.2 AMPERE

AMPERE is a dataset which captures FACs in both the northern and southern hemispheres (Anderson et al., 2000; Waters et al., 2001; Anderson et al., 2014; Waters et al., 2020; Anderson et al., 2021). AMPERE current densities are determined from engineering magnetometers on 66 Iridium telecommunications satellites. The AMPERE dataset is continuous, and provides a map of radial current density in a 1 hour MLT by 1° latitude grid for both hemispheres. Because the Iridium satellites are at 780 km altitude, the full AMPERE grid is resampled every 10 minutes. Spherical harmonic fitting is performed at every 2-minutes over a sliding 10-minute accumulation window (see Waters et al. (2020) for more details), so the data can be provided at 2 minute resolution to aid comparison with SuperDARN data. A review of AMPERE research is available at Coxon et al. (2018). Both the AMPERE dataset and the Spherical Elementary Current System method employed e.g. by Weygand et al. (2023) calculate vertical current density, and using this as a measure of field-aligned current assumes that the field lines are vertical.

The boundary between the R1 and R2 currents (from here on “R1/R2 boundary”) was determined from AMPERE data using the method described by Milan et al. (2015), which will be summarised here. The FAC strength is integrated over circles of different radii and with different circle center locations, and due to the R1/R2 pattern (upward then downward current or vice versa, depending on MLT) a bipolar signature is observed over increasing radius. The circle radius and center location with the largest peak-to-peak bipolar signature is chosen as the circle intersecting the R1 and R2 currents. The latitude at which this boundary intersects the midnight meridian should be equivalent to the boundary where the flows reverse. We have therefore named this the return flow boundary, or in short: R_F .

Using values of R_F provided by Milan (2019), Fogg et al. (2020) determined a linear relationship between R_F and the midnight meridian latitude of the SuperDARN Heppner-Maynard Boundary (HMB). They provide equations to calculate corrected values of the HMB midnight meridian latitude (hereafter referred to as Λ_{Fogg}) based on this linear relationship, which are used to calculate the set of Λ_{Fogg} values (Fogg, 2020) used in this paper. The boundary from Fogg et al. (2020) uses the same standard SuperDARN HMB shape SuperDARN (Shepherd & Ruohoniemi, 2000), because the Fogg method was developed as an alternative to the SuperDARN HMB fitting. The Fogg et al. (2020) fit-

280 ting excluded very active periods, so in this paper we purposefully compare geomagnetic
 281 storms to see if their result can be extrapolated to active periods.

282 3 Results

283 In this section we present data from the three individual event case studies and com-
 284 pare the locations of the SuperDARN-derived HMB (Λ_{Walach}) with the locations of the
 285 R_F boundary and the linear fit for the R_F -derived corrected HMB midnight meridian
 286 latitude (Λ_{Fogg}). These cases are representative of geomagnetic storm times when Λ_{Walach}
 287 goes to lower latitudes than is typical (40-50°) and the number of gridded from Super-
 288 DARN ≥ 250 (Walach et al., 2022a). These three events are fairly representative of fea-
 289 tures we see during highly driven times when Λ_{Walach} moves to lower latitudes and are
 290 good examples at highlighting some of the general issues we face when comparing these
 291 two datasets, which we will discuss in more detail in the following sections.

292 For each event, we show a 48 hour time series. We show four keograms for the AM-
 293 PERE data: with a midnight-noon and a dawn-dusk slice for each hemisphere. This al-
 294 lows us to see rough asymmetries and how the FACs change over time. Λ_{Walach} is over-
 295 laid on top of the AMPERE data alongside Λ_{Fogg} from Fogg (2020) and the R_F bound-
 296 ary (Milan, 2019). Below the keograms we show the difference between Λ_{Fogg} and Λ_{Walach}
 297 and in the last panel we show the geomagnetic conditions: the Sym-H index (Iyemori,
 298 1990), which is an indicator of ring current strength, and the AL and AU indices which
 299 show geomagnetic activity at higher latitudes (Davis & Sugiura, 1966). For each event
 300 we also show a number of polar snapshots. These show the SuperDARN convection maps
 301 and AMPERE data together and they are selected for each event to illustrate specific
 302 points. The SuperDARN convection maps show the electrostatic potentials, Λ_{Walach} ,
 303 and the line-of-sight convection vectors. Overlaid on these polar snapshots is also Λ_{Fogg} .
 304 The full selection of polar plots for all three events are provided in the accompanying
 305 data archive Walach and Fogg (2024a) and the boundaries are available in the suppl-
 306 mentary files by Walach and Fogg (2024b). Anderson et al. (2014) showed that the AM-
 307 PERE data has a three-sigma level of $0.16 \mu\text{A m}^{-2}$, so all AMPERE data below a thresh-
 308 old of $\pm 0.2 \mu\text{A m}^{-2}$ have been plotted in white, and we saturate plots at $\pm 1 \mu\text{A m}^{-2}$
 309 to help bring out reliable features in the data.

310 3.1 Event 1: 20 January 2016

311 Figure 1 shows the four AMPERE keograms for the first case study. Fig. 1a shows
 312 the northern hemisphere midnight-noon slice, Fig. 1b shows the northern hemisphere
 313 dawn-dusk slice and Figs. 1c and 1d show the equivalent slices for the southern hemi-
 314 sphere, respectively. Blue shows downward directed currents whereas red shows upward
 315 directed currents. The green line shows Λ_{Walach} , the black line shows Λ_{Fogg} and the grey
 316 line shows R_F . Fig. 1e shows the difference between Λ_{Fogg} and Λ_{Walach} at midnight in
 317 the northern hemisphere. Fig. 1f shows the geomagnetic conditions for this event: Sym-
 318 H indicates that a small geomagnetic storm occurs, starting on the 20th January and AL
 319 and AU also show a long period of geomagnetic activity, with a series of activations oc-
 320 ccurring at the same time as the Sym-H decrease. Each boundary (Λ_{Fogg} and Λ_{Walach})
 321 will not appear at the same position on each keogram because we took the midnight meri-
 322 dian value, and traced it around the non-circular boundary shape to dawn, dusk, and noon
 323 using the standard SuperDARN formulation (Shepherd & Ruohoniemi, 2000). The dashed
 324 vertical orange lines show the intervals chosen for the polar plots in Figure 2. Prior to
 325 DOY 20.25 (20 January 2016, 06:00 UT) the FACs are, at times, too weak to fit R_F and
 326 so Λ_{Fogg} is also missing at those times in Figure 1. During this time, Λ_{Walach} fits the
 327 latitudinal extent of the existing currents at noon MLT in the southern hemisphere fairly
 328 well. Around DOY 20.25, we see a strengthening of the FACs, as well as an expansion
 329 of the FACs and all boundaries to lower latitudes. After DOY 20.5 (12:00 UT on 20 Jan-

uary 2016) onwards Λ_{Walach} lies at around 5 to 10° lower than Λ_{Fogg} at dawn and dusk (Figs. 1b and 1d) and midnight (Figs. 1a and 1c).

As a general trend for this event, in Fig. 1b, we see Λ_{Fogg} wraps quite tightly around the FACs at dusk and R_F is sometimes just inside the outer edge of the R1 FAC (i.e. more poleward than where it should be). Fig. 1e shows that, generally for event 1, the convective flows are continuing $\sim 7^\circ$ outside Λ_{Fogg} , with the few exceptions which we discussed, when the currents and convection are weak.

Figure 2 shows example snapshots for specifically selected times of interest. These were selected to show a variety of features, and examples where Λ_{Walach} and Λ_{Fogg} fit well or poorly. Figure 2 shows the SuperDARN and AMPERE data plotted in AACGM coordinates (Shepherd, 2014). The time indicates the start of the SuperDARN maps. The blue and red show the AMPERE current density according to the colourbar in the top right, and the black lines show equipotentials from the SuperDARN maps. The line-of-sight SuperDARN flow vectors are shown in green, where lighter vectors show lower magnitudes and darker vectors show larger magnitudes. The black dotted boundary shows Λ_{Fogg} . The thick green line shows Λ_{Walach} , with its midnight meridian latitude recorded on the bottom left of each panel. SuperDARN vectors below Λ_{Walach} are shown in black. Each panel is centered on the northern magnetic pole with noon MLT pointing towards the top of the page, dusk towards the left, midnight towards the bottom and dawn towards the right. Each hour in MLT is indicated by the dashed grey radial lines. The SuperDARN transpolar voltage or cross polar cap potential is shown on the bottom right of each panel. The number underneath (n) indicates the number of backscatter echoes. The cross and red arrow on the top right of each plot shows the projection of the IMF vector on the GSM $Y-Z$ plane. The latitude circles are separated by 10° as indicated by the colatitudes in the top right corner of each panel.

In Fig. 1 we saw Λ_{Walach} lie $\sim 10^\circ$ lower at dawn, dusk and midnight than Λ_{Fogg} and the R2 FACs. In Fig. 2(a), at 13:14 UT on 20 January 2016, we examine this in more detail: Overall, despite the mismatch of Λ_{Walach} lying at lower latitudes than Λ_{Fogg} , the return flow proportion of the convection pattern sits well on R2 FACs. At 15:04 UT (Fig. 2b) we may be seeing something similar to a SAPS signatures included in the convection pattern: We see a current bifurcation of the R2 system at between 3-7 MLT with an eastward directed flow (and a weaker one between 17-20 MLT). Flows continue into the gap between the main R2 and the bifurcation, at $\sim 30^\circ$ colatitude between 6-8 MLT and 2-4 MLT so this could be the start of something similar SAPS event, though we note that SAPS are usually accompanied by westward flows. After this we see repeated bifurcations throughout the interval. As already mentioned during this interval, Λ_{Walach} is around 10° outside the R2 currents. This mismatch happens because the boundary shape does not match the shape of the R2 currents. Later, at around 15:48 UT (Fig. 2c), the convection continues to lie equatorward of the R2 FACs. This expansion is due to an extension of the convective dusk cell across midnight, shifting of the Harang discontinuity towards dawn similar to what was observed during substorms by Bristow et al. (2001, 2003); Bristow and Jensen (2007b).

Later, at 19:48 UT (Fig. 2d) we see persistent, but slow moving flows in the morning sector ($\sim 4-5$ MLT). From Fig.1, we see that the R_F boundary is clearly defined, but we see from Fig.2d that the flows which have defined Λ_{Walach} are sitting far outside R2 (near 6 MLT). Fig. 2e, at 20:20 UT, shows an example of very good agreement: Now, the same vectors which previously defined Λ_{Walach} (between 4 and 6 MLT) are below 100 m/s and therefore fall below Λ_{Walach} , which is now defined by vectors near 7, 11, and 12 MLT. As a result, Λ_{Walach} has moved poleward, wrapping around the FACs nicely, and the two boundaries match perfectly, despite n being lower than for panels a to d. Both Λ_{Walach} and Λ_{Fogg} remain nicely matching for a while after this snapshot (see Fig.1). At 22:10 UT (Fig. 2f) at 13-14 MLT the SuperDARN flows defining Λ_{Walach} lie on top of R2 currents and the boundary-defining flows agree well with the R2 boundary. Due

383 to the boundary shape however, Λ_{Walach} and Λ_{Fogg} do not fit the R2 current bound-
 384 ary at the other MLTs. We note that a circular boundary would fit this interval much
 385 better.

386 Between 23:08 to 23:10 UT (Figs. 2g and h) in the early afternoon sector, the iono-
 387 spheric flows speed up to be above the 100 m/s threshold and therefore Λ_{Walach} shifts
 388 12° in latitude. This shift is much faster than the timescales we would expect, based on
 389 our knowledge of the high-latitude system responses to solar wind driving (e.g. Coxon
 390 et al., 2019), so it is an unrealistic shift. Clearly the currents are also very weakly de-
 391 fined during this time, so it is generally more difficult to see any clear boundary. By 23:20
 392 UT Fig. 2i), the same early afternoon flows helps to define the convection cells nicely around
 393 R1/R2 at dusk, which matches the weak current system.

394 Another feature worth discussing is the sharp change seen in Λ_{Walach} at midnight
 395 just after 06:00 UT on 21 January 2016 (Figs. 2j to l). This can also be seen at day 21.25
 396 in Fig.1a. During the slow expansion following the fast contraction, the agreement be-
 397 tween Λ_{Walach} and the R1 FACs is remarkable in the keograms at midnight at first glance.
 398 At this time however, the AMPERE currents are weak and whilst the sharp change can
 399 be seen in the keograms, the R_F algorithm does not pick up this contraction and con-
 400 sequently, we do not see it in Λ_{Fogg} either. Before the expansion, at Fig. 2j shows Λ_{Walach}
 401 equatorward of Λ_{Fogg} but it is clear that neither is well defined here: n is very low ($n=4$)
 402 and the currents are weak. In Fig. 2k we then see that although the currents weaken and
 403 shrink after the contraction at 06:24 UT, this is not as dramatic as the change in Λ_{Walach} ,
 404 which is defined by less than 10 SuperDARN vectors and a poor quality fit. During this
 405 contraction and expansion, the Λ_{Walach} matches well with the edge of R1 at midnight,
 406 but slow flows mean that Λ_{Walach} is poorly defined, despite weak currents. As the con-
 407 vection pattern shrinks abruptly and then slowly expands again, the R2 is outside Λ_{Walach}
 408 for several hours. We also note that at the same time, R2 lies far equatorward of R1 at
 409 most MLTs. At 09:40 UT (Fig. 2l) we show the convection pattern once it has expanded
 410 again and Λ_{Walach} is equal to Λ_{Fogg} . Despite the good match, there are still very few
 411 SuperDARN vectors ($n=29$), but the pattern is constrained correctly by a few vectors
 412 at 1 MLT.

413 3.2 Event 2: 20 December 2015

414 Figure 3 shows the AMPERE keograms for an interval of multiple substorm on-
 415 sets. In this case the boundaries expand and contract with the FACs overall, with ma-
 416 jor disagreements between the FACs and the boundaries in the northern hemisphere dawn
 417 sector. This is an interesting interval, as there is some dayside driving and Λ_{Walach} is
 418 at low latitudes for a long time (\sim half a day), whilst geomagnetic storm occurs, which
 419 is shown by the decrease in Sym-H in Fig.3f. During this interval we see some classic sub-
 420 storms in the FACs in the keograms, seen in the sawtooth-like expansions and contrac-
 421 tions of the FACs at dawn (e.g. 354.25 DOY or 354.65 DOY and onwards) and accom-
 422 panied by enhancements in AL in Fig.3f. We note that the boundaries do not always fol-
 423 low these expansions and contractions, which are less strongly observed in the R2 cur-
 424 rent systems than in the R1 currents. R_F does not pick up most of the expansions and
 425 contractions, which is surprising, given that they are so clear in R1.

426 Throughout the middle section of the event, Λ_{Walach} expands further outside the
 427 FACs than Λ_{Fogg} and R_F , as seen in Fig. 3. Fig. 3e shows that the difference between
 428 Λ_{Fogg} and Λ_{Walach} is positive for most of this event, which means Λ_{Walach} lies equator-
 429 ward. This is due to SuperDARN registering scatter equatorward of the R2 FACs. This
 430 poses the philosophical question if the convection boundary should be the lower bound-
 431 ary of "polar convection" (i.e. Dungey cycle-driven) or all convection. Even flow shears
 432 produced by "sub-auroral" or "mid-latitude phenomena" should have FACs associated
 433 with them, so we argue that these should be included. The issue we are seeing with this

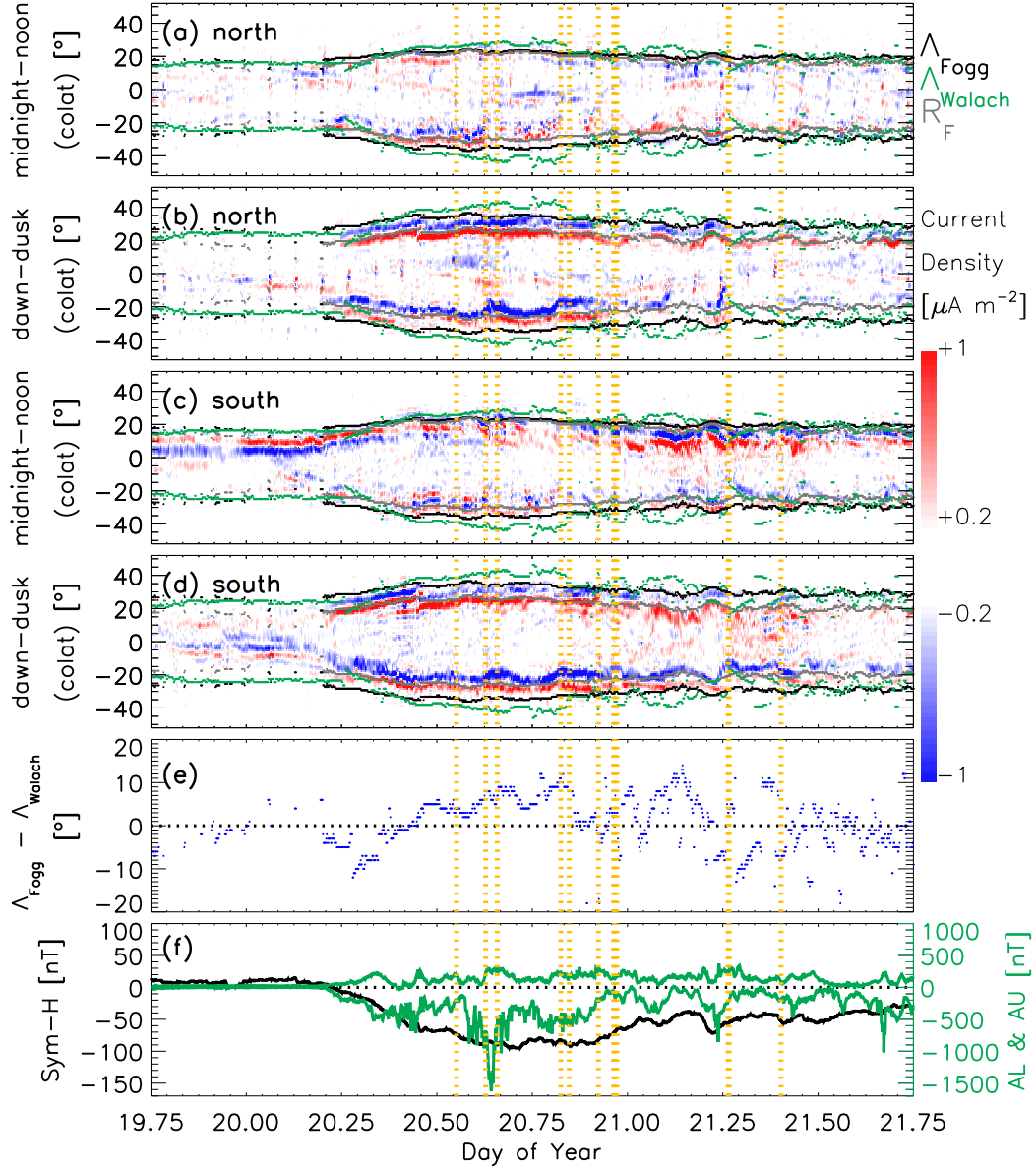


Figure 1. Six panelled plot showing keograms of the FACs and flow boundaries for 18:00 UT on 19 January 2016 to 18:00 UT on 21 January 2016: Λ_{Walach} (green), Λ_{Fogg} (black) and R_F (grey). The vertical dashed orange lines indicate the timings for the panels in Figure 2. a) and c) show the midnight-noon keograms for the northern and southern hemisphere, respectively. b) and d) show the dawn-dusk keograms for the northern and southern hemispheres, respectively. Fig. 1e) shows the difference at midnight between Λ_{Fogg} and Λ_{Walach} in the northern hemisphere and panel f) shows the geomagnetic conditions: Sym-H (black), and AL and AU (green). Each minor tick on the horizontal axis is equivalent to one hour and the major ticks are separated by six hours each.

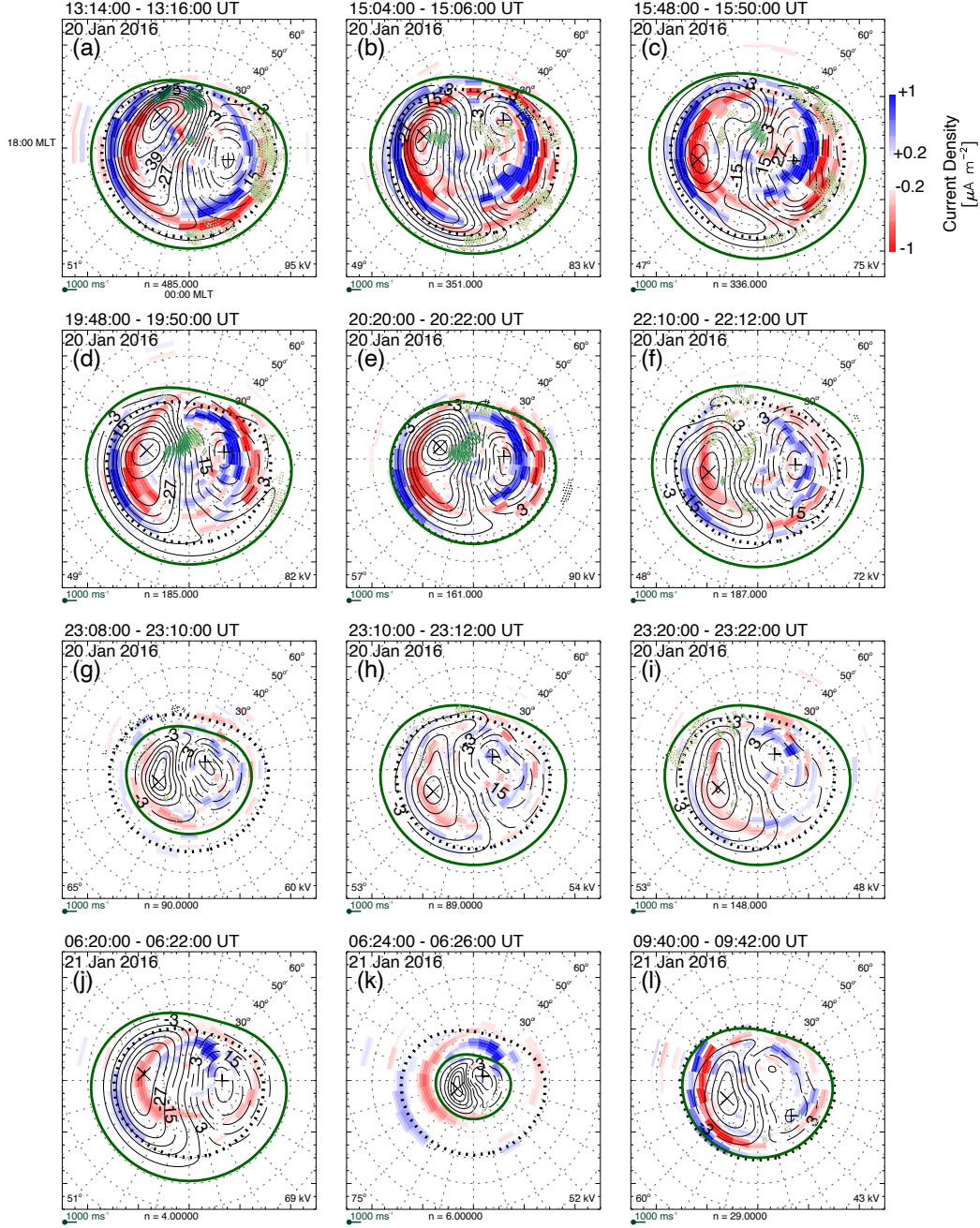


Figure 2. Example snapshots of the polar view for Event 1: Each panel is centered on the northern magnetic pole with noon MLT pointing towards the top of the page, dusk towards the left, and midnight towards the bottom, as indicated on (a). The top left of each panel indicates the time and date of the snapshot. The colours show the AMPERE data (red=upwards current, blue=downwards current, FACs saturate at ± 1 micro A m^{-2}) and the SuperDARN line-of-sight flow vectors, going from light green (slow flows) to dark green (fast flows). Vectors outside of Λ_{Walach} are shown in black. The thick green boundary shows Λ_{Walach} and the thick black dotted boundary shows Λ_{Fogg} . The equipotentials are overlaid in thin black lines. The number on the bottom left of each plot gives the latitude of Λ_{Walach} at midnight for reference and the number on the bottom right gives the polar cap potential. n shows the number of total SuperDARN vectors in each map. The latitude lines are separated by 10° and the outer co-latitudes are labelled in the top right corner of each panel.

434 interval is that although we measure flow shears at lower latitudes, there are only very
 435 weak FACs, suggesting either an issue with measuring FACs at these lower latitudes, pos-
 436 sibly due to the change in magnetic field geometry. We will revisit this philosophical ques-
 437 tion in more detail in the discussion section.

438 Figure 4a shows a snapshot at 16:10 UT (20 December 2015). This shows a strong
 439 FAC pattern (with currents stronger than $1\mu Am^{-2}$) and a strong convection pattern (CPCP=154kV)
 440 with an extension of the dusk cell across the nightside. We also see an extension of the
 441 R1 dusk currents across midnight and merging with the R2 currents on the dawnside,
 442 which matches the extension of the convection cell, but the extension of the currents is
 443 observed at a higher latitude than Λ_{Walach} . From visual inspection, we would expect Λ_{Walach}
 444 to perhaps lie at a slightly higher latitude, but we find that this is defined by the scatter
 445 in the 11 MLT region and this moves Λ_{Walach} to lower latitudes at other MLTs due
 446 to the asymmetric shape of the boundary. This is a feature which re-emerges through-
 447 out the interval: Dayside scatter being located at lower latitudes generally pushes Λ_{Walach}
 448 down such that it erroneously lies below the current system's locations on the nightside.
 449 This issue is exacerbated by the non-circular shape of the traditional HMB, and places
 450 a question over whether this is the correct shape to be using.

451 At 17:52 UT (20 December 2015, Fig. 4b) we still see the extension of the dusk cell
 452 across midnight but any FACs in this region are too weak to match this flow feature. Whilst
 453 Λ_{Fogg} fits the equatorward boundary of the observed R2 currents well, it consequently
 454 lies poleward of the midnight sector convection. Λ_{Walach} is still approximately 10° equa-
 455 torward. This location seems reasonable on the dayside but appears to be too far equa-
 456 torward at other local times. It is evident that a circular shape for the HMB would solve
 457 this problem and fit much better here. At 18:38 UT (20 December 2015, Fig. 4c) the scatter
 458 places Λ_{Walach} at 50° , which matches the R2 boundaries well, especially at dusk and
 459 midnight. On the duskside, Λ_{Fogg} lies more poleward and on top of the R2 currents (blue).
 460 At midnight Λ_{Fogg} lies just poleward of a faint upward current (red), which we judge
 461 to be equatorward of the R2 currents; the R2 currents look to be just poleward of Λ_{Fogg} .
 462 Λ_{Walach} is just equatorward of the same faint upward current. In general the midnight
 463 sector currents are quite complex at this time and we suggest they are possibly substorm-
 464 related as shown by the contractions and expansions in the FACs. There is a slight asym-
 465 metry in the currents between dusk and dawn with the dawn boundary being closer to
 466 the pole. This presents a difficult match with a boundary shape that is symmetric with
 467 respect to dusk and dawn as is the case for both boundaries shown. At 13:38 UT (21st
 468 December 2015, Fig. 4d), we see the R2 currents on the duskside (blue outer circle) bi-
 469 furcated, but nevertheless, Λ_{Fogg} and Λ_{Walach} are at the same latitude.

470 Generally in this interval, Λ_{Fogg} wraps around the currents more tightly at dusk
 471 than at dawn, and sometimes fits the extent of the current system nicely on the night-
 472 side as well. Overall, Λ_{Walach} tends to lie more equatorward, due to the dayside scatter
 473 pushing the boundary equatorward. Despite the mismatch in boundary locations,
 474 Λ_{Walach} , judged on its own, would be considered to be well-defined due to the large num-
 475 ber of scatter points.

476 3.3 Event 3: 15 July 2012

477 Figures 5 and 6 are laid out in the same way as the previous plots but for event
 478 3, which shows a strongly driven interval and a geomagnetic storm. Fig. 5f shows Sym-
 479 H decreasing to ~ 100 nT which indicates that a geomagnetic storm is underway. AL and
 480 AU are also enhanced at the same time and we see a number of rapid enhancements in
 481 AL, which indicate a series of substorms. We see from Figure 5 that this is a very ac-
 482 tive interval with strong currents. We will return to Fig. 5 after discussing a few spe-
 483 cific polar snapshot examples from Fig. 6.

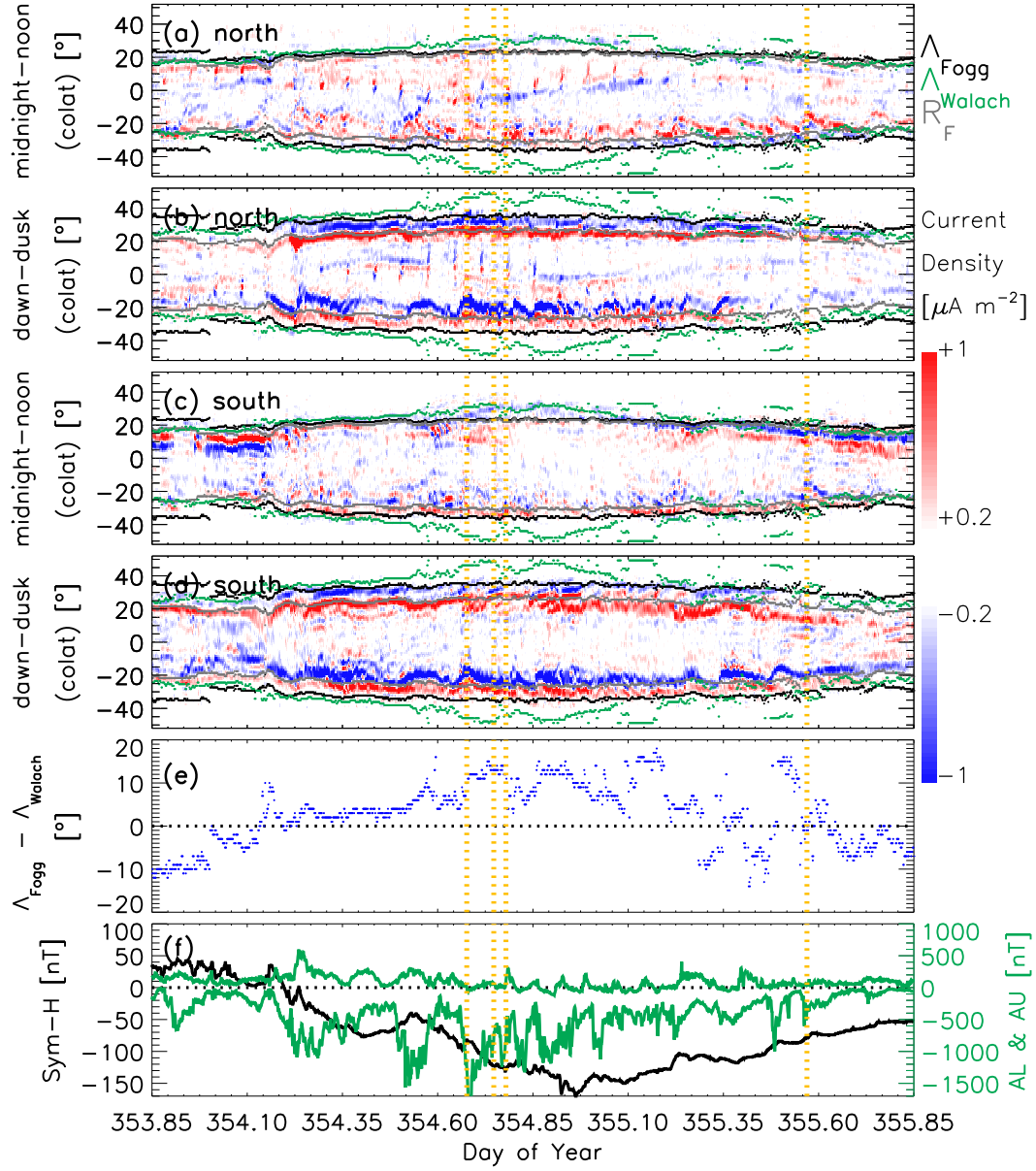


Figure 3. Six panelled plot showing keograms of the FACs and flow boundaries for 20:20 UT on 19 December 2015 to 20:20 UT on 21 December 2015 in the same format as Fig.1.

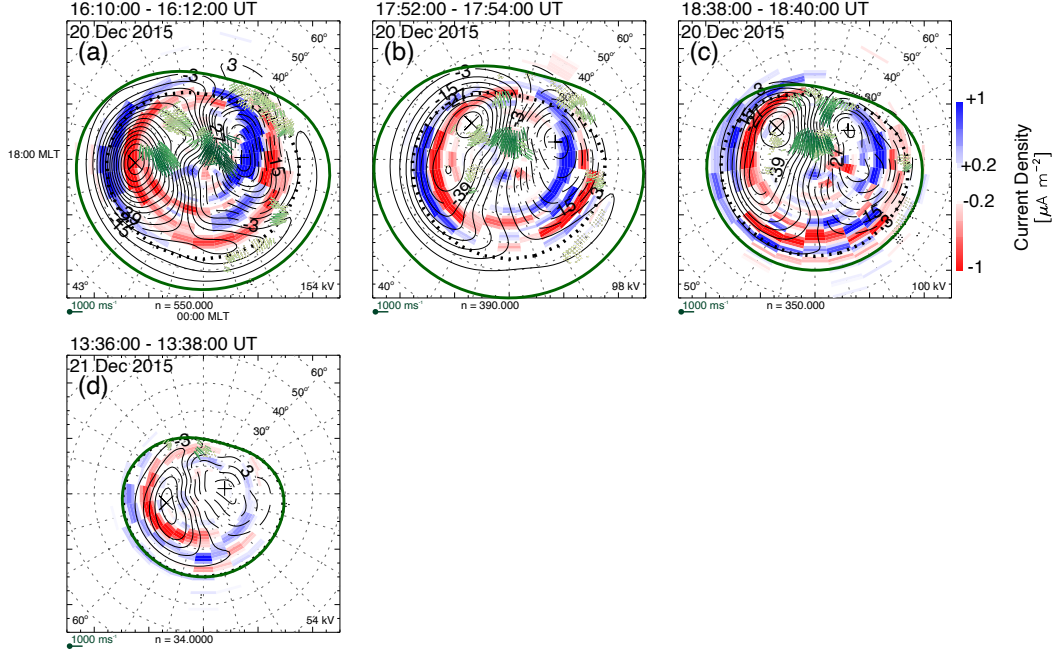


Figure 4. Example snapshots of the polar view for Event 2 in the same format as Fig.2.

484 Right at the beginning of the interval (14 July 2012 at 23:00 UT Fig. 6a), Λ_{Walach}
 485 is poleward of Λ_{Fogg} due to insufficient vectors at lower latitudes. On 15 July 2012 after
 486 $\sim 07:28$ UT, enhanced dawn-dusk currents occur. Fig. 5 shows that these dawn-dusk
 487 currents are not always symmetric around the pole, especially at dusk, where the cur-
 488 rents are weaker. Coxon et al. (2023) also saw a systematically reduced probability of
 489 current density on the dusk side in comparison to the dawn side, which highlights an issue
 490 with fitting symmetric boundaries. Despite the weak currents, Λ_{Walach} fits the loca-
 491 tion of the currents well (see 07:28 UT Fig. 6b). At 10:24 UT (Fig. 6c), a bifurcation
 492 has developed on the nightside. At this point the R2 dawn currents have bifurcated and
 493 form a separate feature on the nightside (23-5 MLT). Unfortunately, we measure no Super-
 494 DARN scatter around the bifurcation, and the number of gridded SuperDARN vectors (n)
 495 is very low (82, see (Walach et al., 2022a) for how this compares to this dataset
 496 in general). At 12:00 UT on 15 July 2012 (see Fig. 5 and Fig. 6d) strong R0 currents
 497 are observed but there is little co-located SuperDARN scatter observed. During this time,
 498 the R2 currents on the dayside (early afternoon sector) are very strong and located over
 499 a wide area, but there is very little SuperDARN scatter located in this area, so Λ_{Walach}
 500 is poleward of the dayside FACs. Λ_{Fogg} lies even more poleward and matches the R2 bound-
 501 ary well around the nightside but neither Λ_{Walach} or Λ_{Fogg} agree with the currents at
 502 12:00 UT.

503 Later, at 22:44 UT (Fig. 6e), Λ_{Walach} fits the afternoon sector well, being well de-
 504 fined by SuperDARN scatter. We also see a weak R2 bifurcation in that region (~ 15 MLT),
 505 which matches the location of fast scatter. The R2 at ~ 6 MLT also undergoes a faint
 506 bifurcation which reaches around midnight to dusk and this bifurcation persists for some
 507 time (Fig. 6f). The bifurcated feature becomes the outer edge of the current system and
 508 Λ_{Fogg} matches this too. The next day, at 12:08 UT (panel g), the previous current bifur-
 509 cation has disappeared but the current system is still complex. Λ_{Walach} and Λ_{Fogg}
 510 are only offset by a degree or two and both hug the current systems on the nightside.
 511 Due to the shape of the boundaries and the circular-shaped current system on the day-
 512 side, however, both boundaries do not manage to hold all the currents within.

Overall during this event, Λ_{Walach} reaches 40° but Λ_{Fogg} does not. This is for example seen in all panels in Figure 5 at around DOY 198 (and in Figs. 6e and f at 22:44 UT on 15 July 2012 and 00:00 UT on 16 July 2012, respectively) due to a long period of dayside driving, which drives Λ_{Walach} to low latitudes and means Λ_{Walach} is generally equatorward of Λ_{Fogg} . Here, Λ_{Walach} is fitted to scatter on the dayside, and it captures the dayside currents well as a result, but the boundary falls far outside the currents at other MLTs. The fit is particularly poor on the nightside where the currents are weaker and the early afternoon where some currents are outside Λ_{Walach} and Λ_{Fogg} . This is another example of an interval where a circular fit to the convection boundary may be more appropriate (e.g. see also Fig. 2f and Fig. 4a).

In this interval we also see some instances where the FACs contract but the convection pattern (observed by SuperDARN and quantified by Λ_{Walach}) contracts more slowly. For example, at DOY ~ 198.5 (see 12:08 UT on 16 July 2012 in Fig. 6g and region around last vertical dashed orange line in Fig. 5) in the dawn/dusk currents (Fig. 5b and d) we see an example of a quick and sharp change in the currents which is picked up by R_F and hence Λ_{Fogg} . The convection data however, and with it Λ_{Walach} responds more gradually. When we look at this in a polar view (Fig. 6g), it looks like the FAC semi-circle has been shortened on the dusk side, so the dusk R2 FACs are now restricted to the noon/afternoon sector and end near dusk, as opposed to being centred on the dusk meridian. Whilst Λ_{Walach} does not match Λ_{Fogg} during this contraction at around 12:08 UT, we emphasize that this is a non-standard case as the dusk-side currents are usually centred on the dusk meridian but here they are not.

Overall, during this interval, the dawn-dusk wedges fit Λ_{Fogg} well, whereas at noon this boundary sometimes sits at higher latitudes than where the FACs terminate.

3.4 Statistical Overview

Figure 7 shows a statistical overview of the latitudinal offset between the boundaries at midnight $\delta\Lambda = \Lambda_{Fogg} - \Lambda_{Walach}$ plotted against the number of gridded SuperDARN vectors per SuperDARN map n . Each panel shows one of the three events and the data are represented as a scatter plot over a continuous probability density distribution. The vertical lines show the median (black solid), mean (black dotted) and 0° (grey dashed). In all three events, we see that on average, $\delta\Lambda > 0^\circ$, which means Λ_{Walach} generally lies equatorward of Λ_{Fogg} .

Fig. 7 also shows that the only times when $\delta\Lambda < 0^\circ$ (such that Λ_{Fogg} is equatorward of Λ_{Walach}) occur when n is not very high (e.g. mostly less than 200). In general, when n is high, $\delta\Lambda$ tends to be greater than 0.

The probability density curves on the x- and y-axis show that a large proportion of the data (45.9%, 64.0% and 50.0%, respectively per event) is distributed in the region $0^\circ \leq \delta\Lambda \leq 5^\circ$ for all three events, suggesting that the two boundaries usually match well. On average, Λ_{Walach} sits $\sim 3^\circ$ equatorward of Λ_{Fogg} .

The first event has a secondary peak in $\delta\Lambda$ on the probability density curve at the top. This secondary peak lies to the left of the main peak when $\delta\Lambda \leq 10^\circ$ and n is low (less than 100). The implication of this is that when n is low, Λ_{Walach} can be at higher latitudes than Λ_{Fogg} . These are likely times when the boundary is poorly identified by SuperDARN data.

We also note that the overall form of the distribution of the two right hand (pink, purple) plots are more similar to each other than the left hand plot (red). This is likely due to the fact that events 2 and 3 are more driven and have stronger geomagnetic storms whereas the first event has a weaker geomagnetic storm.

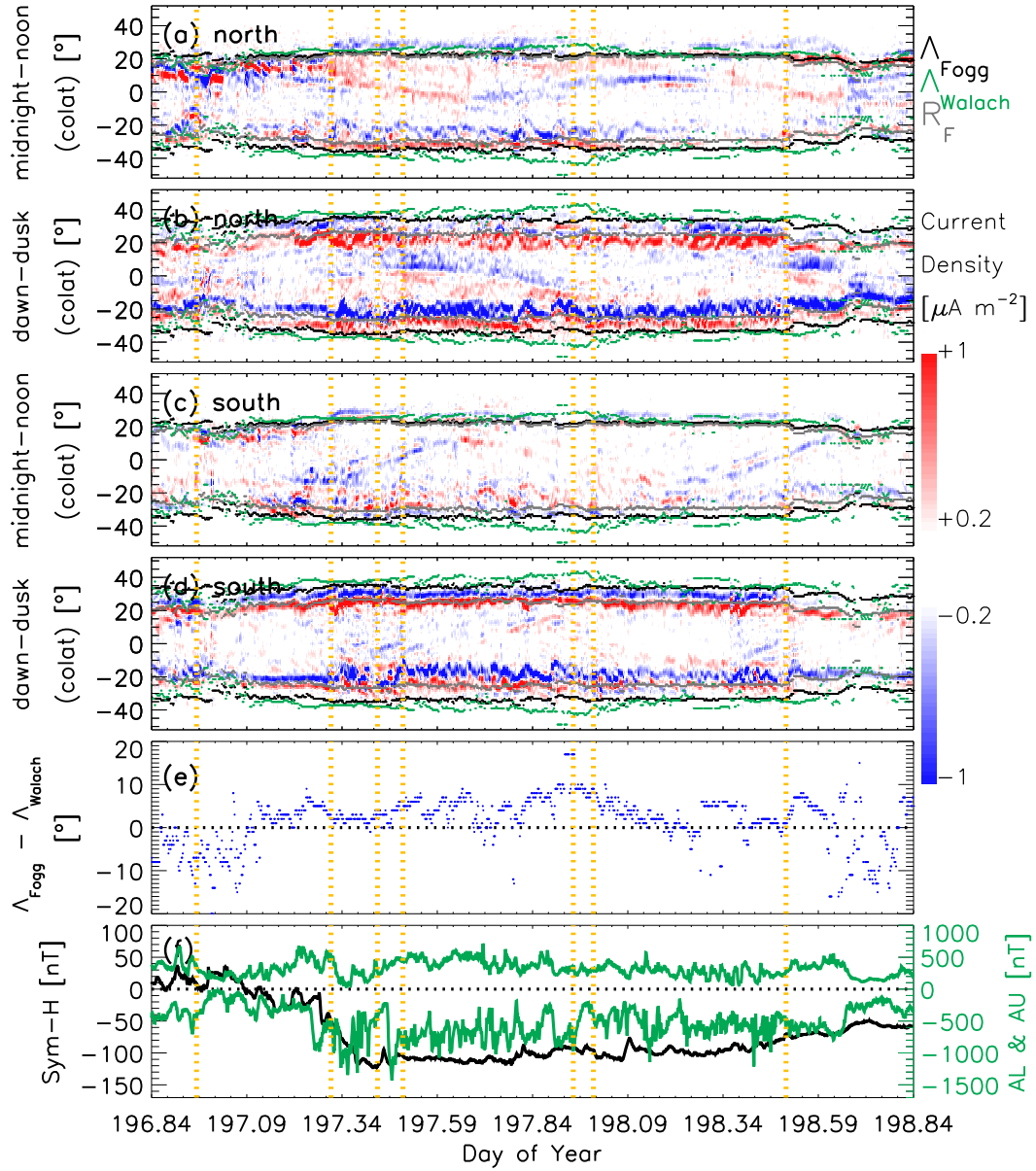


Figure 5. Six panelled plot showing keograms of the FACs and flow boundaries for 20:10 UT on 14 July 2012 to 20:10 UT on 16 July 2012 in the same format as Figs.1 and 3.

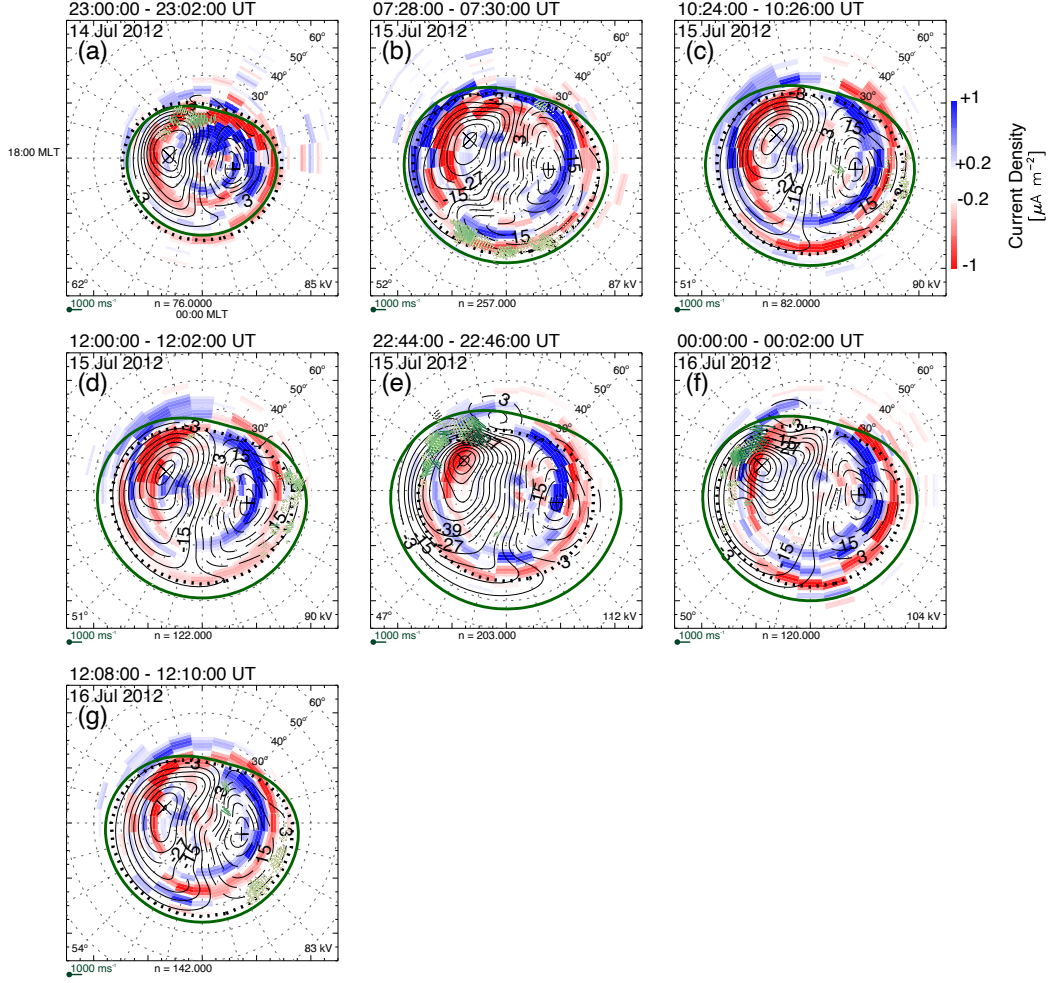


Figure 6. Example snapshots of the polar view for Event 3 in the same format as Fig.2 and 4.

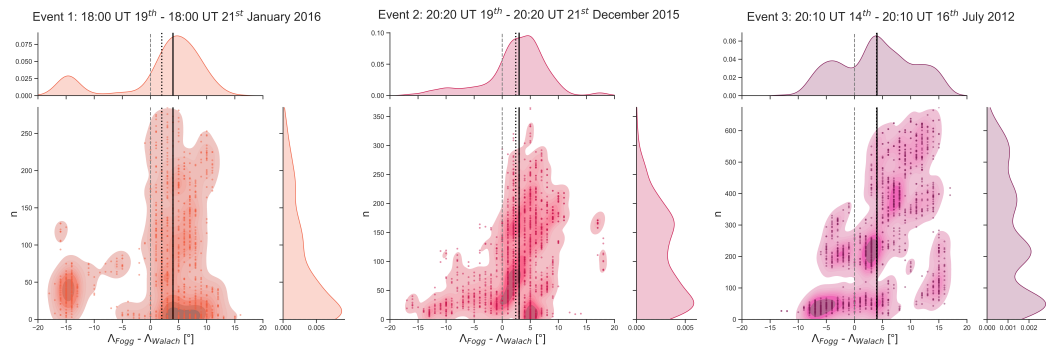


Figure 7. Three panelled figure showing the statistical distribution of the latitudinal offset between the boundaries at midnight, $\Delta_{Fogg} - \Delta_{Walach}$, against n for each event. The coloured contours show a continuous probability density curve for each event distribution with the overlaid scatter showing the individual observations. The black solid line shows the median in $\Delta_{Fogg} - \Delta_{Walach}$ and the dotted black line shows the mean. The grey dashed line shows 0° difference.

4 Discussion

The key question which we set out to answer in this study was: How reliable is the FAC boundary location at picking up the same boundary as SuperDARN for the ionospheric convection boundary? We investigated this for geomagnetic storm conditions as this causes the convection boundary to move to latitudes as low as 40° (Walach & Grocott, 2019) and latitudes below 50° were not explored by Fogg et al. (2020). In the reference frame of the neutrals, there have to be FACs at the shear of convective flows. We have found that for reasons of data quality this is not always the case. Overall, we find that Λ_{Walach} is more likely to lie equatorward of Λ_{Fogg} than the other way around. We discuss the reasons for this in the following section.

The primary reason why Λ_{Fogg} and Λ_{Walach} disagree with each other or the FAC locations is the geometry. The geometry of the standard SuperDARN boundary and the geometry of the FACs as measured by AMPERE are often in disagreement and this makes it a difficult comparison. This plays a key role in the disagreements we have uncovered. The shape of the HMB used in the SuperDARN fitting, and thus Λ_{Walach} is based on a statistical study by Heppner and Maynard (1987). Shepherd and Ruohoniemi (2000) surveyed SuperDARN data and found that the ovoid shape proposed by Heppner and Maynard (1987) was a better fit than the circle, which was used previously for the HMB-shape. This ovoid is circular along the nightside edge and indented towards the pole on the dayside. The dayside indentation matches our understanding of the magnetospheric geometry: on the dayside it is pushed into a bow-shape by the solar wind. A question that has arisen from studying these data however is: Is the SuperDARN HMB the correct shape? In some cases (e.g. Fig. 4b and all panels in Fig.6), a completely circular shape would perhaps fit the AMPERE data better, but not in all cases. Another geometrical issue arises from the azimuthal asymmetries (e.g. Fig. 4c at 18:38 UT Λ_{Walach} fits the AMPERE current boundary well, but on the dawnside, the AMPERE currents terminate at a higher latitude). Whilst we have not found a systematic MLT dependence of the relationship between R_F or Λ_{Fogg} and Λ_{Walach} (since this is out of the scope of this study), it is certainly clear that at different times these exist and that a circular fit for the convection boundary would therefore not always be ideal. Furthermore, Λ_{Fogg} relies on the R_F fit from Milan (2019). Due to geometrical reasons (e.g. the currents are weak or the R2 FAC regions unusually wide), R_F may be poorly constrained and therefore Λ_{Fogg} may also be poorly fitted.

Data are needed to ascertain the Λ_{Walach} placement in the standard SuperDARN fitting but the primary limitation is the coverage. For example, in many cases there is little backscatter observed equatorward of the dayside boundary, which makes this identification difficult. One way to use data for boundary selection is to use AMPERE data as was done for Λ_{Fogg} . This comes with its own challenges: As we have shown, sometimes the data do not agree and whilst the fitted AMPERE boundaries (R_F) are circular, the morphologies of the FACs are not necessarily circular (or fitting to the functional SuperDARN HMB form) either. We have also seen a number of cases where the convection pattern expands or contracts and these boundary movements are out of step with each other. We have seen examples in every one of the three events, where the AMPERE pattern contracts and the contraction in the SuperDARN convection pattern is delayed. This suggests there are some feedback effects in the ionosphere, which could be a sign of a delay in the communication times between currents and convection or a sign of sensitivity issues with the temporal/spatial cadence of AMPERE. Expansions are mostly in time with each other, but there are also examples when the AMPERE pattern expands very rapidly and this is not reflected in the SuperDARN pattern. Most likely, changes reflected in the AMPERE FACs or SuperDARN convection are due to changes in one local time which affect the global fitting. For example, we see such changes from Fig. 2d to 2e), where the SuperDARN measurements at ~ 4 MLT are at first included in the con-

613 vection pattern but then fall below the Λ_{Walach} boundary due to slow scatter on the day-
 614 side fixing Λ_{Walach} in Fig. 2.

615 Whilst the main limitation of the SuperDARN-method of determining the convec-
 616 tion boundary (Λ_{Walach}) is data availability, the Fogg-method of determining the bound-
 617 ary (Λ_{Fogg}) brings its own challenges. We find that when the currents are very weak (e.g.
 618 at the beginning of event 1), the R_F boundary cannot be found, whereas the SuperDARN
 619 data can find and constrain the convection boundary. In this case, one could apply the
 620 Fogg-method to averaged maps of AMPERE data but this is still likely to yield no bound-
 621 ary when currents are weak. Instead, one could use the SuperDARN boundary when no
 622 boundary can be derived from AMPERE.

623 Imber et al. (2013b) previously studied how the HMB moves with the auroral oval.
 624 They found that by smoothing the HMB latitude across time, and comparing this to the
 625 brightest part of the auroral oval, the HMB lies just a few degrees equatorward of the
 626 auroral oval. Whilst this is reflected by some of our results, we caution against such a
 627 generalization: Our data clearly shows that there is complexity in the data that cannot
 628 be summarized by a simple relationship. Furthermore, Imber et al. (2013b) used data
 629 from 2000-2002, but during this time, the SuperDARN fitting was not able to place the
 630 HMB below 50° geomagnetic latitude due to limited radar coverage (Walach & Grocott,
 631 2019), so it is not a useful comparison for our study which exclusively has focused on ge-
 632 omagnetic storms. To add further context to the equivalence of the auroral oval and FACs,
 633 we point the reader to Carter et al. (2016) who showed that the statistical distribution
 634 of FACs is not necessarily a good indicator of auroral location.

635 According to the diagram in Figure 2 of Milan et al. (2017) (see also e.g. Cowley,
 636 2000), convection happens between R1 and R2 FACs. This assumes that the neutral at-
 637 mosphere is stationary in reference to the electric fields. We observe convection on the
 638 R2 FACs or, when current bifurcations are present, on a R2 bifurcation, or indeed be-
 639 tween the R2 and the bifurcation. Often, the return flows also occur on the R1 FACs,
 640 which also does not match the cartoon from Milan et al. (2017) and therefore our un-
 641 derstanding of the electrodynamics. We put forward two reasons for this. On a statisti-
 642 cal level, the Λ_{Fogg} and Λ_{Walach} compare well, but as we have shown, over just three
 643 short events, there can be a large amount of discrepancy (up to 20°). This discrepancy
 644 tends to be larger when the number of backscatter echoes in the SuperDARN maps is
 645 lower, suggesting that this is primarily due to uncertainty in identifying Λ_{Walach} when
 646 data coverage is lower. We have shown that, on average, Λ_{Walach} sits at lower latitudes
 647 than Λ_{Fogg} with a systematic offset of $\sim 3^\circ$. This compares to the root mean square er-
 648 ror found by Fogg et al. (2020) (2.75°), who correlated the HMB at midnight with R_F .
 649 We also find, however, that the latitudinal difference between the two boundaries is not
 650 always systematic and it is not possible to choose which boundary fitting (Λ_{Fogg} or Λ_{Walach})
 651 is best overall. This also shows that there is a deeper gap in our understanding which
 652 goes beyond the geometries of the data fitting and the magnetosphere-ionosphere sys-
 653 tem: If the AMPERE and SuperDARN data do not match in their dynamic signatures,
 654 there is something missing. This is most likely related to the data processing (both datasets
 655 undergo a number of fitting steps), it could be a physical decoupling between the alti-
 656 tude at which the data are sampled (e.g. SuperDARN and AMPERE are obtained at
 657 ~ 300 km and ~ 780 km, respectively). A key assumption that is often made is that the
 658 conductivity is uniform. Since the conductivity relates ionospheric vorticity and the field-
 659 aligned current strength, it is also likely that uniform conductivity is a poor assumption.
 660 In any case, it is a gap in our understanding.

661 No data processing technique is perfect. Missing SuperDARN backscatter often means
 662 the maps are constructed by extrapolating the background model and Λ_{Walach} from MLT
 663 sectors with data coverage to MLT sectors with no scatter. This has the benefit that maps
 664 can be constructed without fully global data coverage but it does also mean that care
 665 has to be taken with interpreting the maps. Currently, there is no established way of as-

666 sassing convection map quality beyond the number of vectors and this is something that
 667 needs to be established (e.g. see discussion by Walach et al., 2022a). There could be er-
 668 rors in the geolocation of SuperDARN scatter, which could put velocity shears into the
 669 wrong place but we have minimised this in our data processing technique as described
 670 in Walach et al. (2022a).

671 Indeed, there is currently no way to verify “best” fit or latitude position for the HMB
 672 for any given map, independent of SuperDARN scatter availability. Fogg et al. (2020)
 673 sought to overcome dependence on scatter availability by using an independent data source
 674 (AMPERE) to define the equatorward boundary of convection. In this study we show
 675 some agreement, and some disagreement between boundaries using the method of Fogg
 676 et al. (2020) and the traditionally determined HMB. Along with our observations on the
 677 shape of the HMB, and uncertainty in the types of flows, this generates important ques-
 678 tions for the community: how best can we define the equatorward edge of the convec-
 679 tion pattern, and what types of flows should we include in this convection pattern? For
 680 example, should it only include Dungey-driven convection or also sub-auroral phenom-
 681 ena?

682 The ionosphere does not always truly become stationary at latitudes below Λ_{Walach} ,
 683 even in the rest frame of the neutrals. There are published results with SuperDARN in-
 684 dicated that, in addition to SAPS, reduced, but still finite, flows continue below that
 685 boundary (Maimaiti et al., 2019). In whole atmospheric modelling communities, how-
 686 ever, and even magnetospheric physics, the electric fields generated by the Dungey-driven
 687 convection pattern and lower latitudes are thought of as two separate “fields”. It is how-
 688 ever not conducive to think of these as separate since all shear flows should be associ-
 689 ated with FACs, unless the magnetosphere-ionosphere are no longer coupled. Further-
 690 more, the SuperDARN fitting technique was designed to encompass all flows since they
 691 all have to be incompressible and must map to plasma convection in the magnetosphere,
 692 which is communicated by FACs. Due to limitations in radar coverage, SuperDARN back-
 693 ground models did traditionally not include mid-latitude or sub-auroral phenomena, but
 694 it is crucial that this is advanced, since all convection should be captured with the con-
 695 vection maps. Especially when we discuss features such as bifurcations (Sangha et al.,
 696 2020) and SAPS (e.g. Foster & Vo, 2002; Kunduri et al., 2018), which are often observed
 697 together (Sangha et al., 2020), and originate in the return flow part of the traditional
 698 two-cell pattern (Sangha et al., 2020), so they are an integral part to convection. Sangha
 699 et al. (2020) showed that this is a phenomenon that commonly occurs during substorms.

700 Whilst it might be a challenge, we must incorporate SAPS and bifurcations in the
 701 convection maps and improve the fitting techniques to be able to do so without compro-
 702 mising overall quality. Λ_{Walach} is more likely to be influenced by mid- to low-latitude
 703 phenomena, but as we have shown, current bifurcations occur frequently and should not
 704 be dismissed as a mere outlier. The biggest question surrounding these features is where
 705 in the magnetosphere the FACs associated with these flows close and to answer this ef-
 706 fectively, we must be able to map the bifurcations and SAPS alongside all other currents
 707 and flows.

708 We have alluded to the fact that the equatorward extent of the convection and the
 709 FACs can be decoupled. In summary, we have discussed the uncertainties around conduc-
 710 tivity, geometry, data processing methods, time-varying phenomena such as SAPS
 711 and possibly inductive effects which can offset these boundaries. We further add that
 712 if the response times of the convection and FACs are different, the data may appear de-
 713 coupled due to the sampling rate, but the electrodynamics have to be consistent. We con-
 714 clude that conductivity gradients would be the most likely factor in generating an ob-
 715 served inconsistency between FACs and the convection: it is possible that FACs would
 716 preferentially close at higher latitudes through regions of high conductivity (e.g. in the
 717 auroral regions), whilst convection can continue at lower latitudes in regions where the
 718 currents do not propagate as easily.

5 Summary

In this article we have presented three case studies to observe and compare the SuperDARN-derived HMB (Λ_{Walach}) and the equivalent boundary of the FACs (Λ_{Fogg}). The purpose of this was two-fold: Firstly, we compare Λ_{Walach} to a newer method from Fogg et al. (2020). The Fogg et al. (2020) method used a statistical AMPERE database to develop an empirical model for the FAC boundary, whereas Λ_{Walach} chooses the boundary based on the lowest latitude at which the flow vectors approach 0 m/s. Secondly, the purpose of this study was to compare the boundaries to the FACs themselves. This is not necessarily the same as Λ_{Fogg} , as Λ_{Fogg} relies on a fit between the R1 and R2 currents. With our case studies, we have established how well the different boundaries match each other, but also, and perhaps more crucially, find instances when they do not match. These are important and novel results as, theoretically, the boundaries should match (e.g. Milan et al., 2017).

Overall, our observations show the following:

- Agreement between Λ_{Fogg} , the FAC-derived boundary, and Λ_{Walach} , the flow-derived boundary is likely to be best when the SuperDARN data coverage is high.
- On average, Λ_{Walach} is $\sim 3^\circ$ equatorward of Λ_{Fogg} .
- Poor agreement between the Λ_{Fogg} and Λ_{Walach} comes from either: 1) Not enough scatter at different latitudes and MLT, which leads to poor fitting; 2) Deformations such as bifurcations/asymmetries in the FAC pattern.
- During geomagnetically active times, a circular HMB may present a better fit.
- Instances where Λ_{Walach} and Λ_{Fogg} match each other on the dayside but not on the nightside (and vice versa) and fit well at dusk but not dawn (and vice versa), happen often. This is mostly due to late morning scatter which has defined Λ_{Walach} , and is colocated with the currents. This does however lead to Λ_{Walach} being at much lower latitude on the nightside than Λ_{Fogg} and is one of the main reasons for poor agreement on the nightside.
- Most often Λ_{Walach} fits the Λ_{Fogg} best in the dusk/afternoon sector.
- Sometimes Λ_{Walach} sits at lower latitudes than the currents because the return flows are observed below the R2 FACs or the flows sit on a FAC bifurcation.
- If there is an offset between Λ_{Walach} and FAC pattern, it is around $3\text{-}5^\circ$; and in cases where this occurs, the convection cells fit well around the FACs, but the return flow region stretches to lower latitudes.
- Λ_{Fogg} does not always follow the expansions/contractions in the FACs. Λ_{Fogg} relies on the R1/R2 boundary being fitted well and this is not always the case for expansions/contractions of the current system.
- Most of the sharp contractions in the current systems are not shown in Λ_{Walach} . This is either because the scatter disappears (and it is therefore not measurable) or Λ_{Walach} is more slow to respond, which may be due to inertial coupling between the neutrals and ions at a lower altitude to AMPERE, and AMPERE is therefore not sensitive enough to pick up.

It is clear that no dataset is perfect and this is important to discuss and keep in mind. A crucial factor is the data processing. We have shown that the shape used for the fitting is not always appropriate. Sometimes, a more asymmetric boundary would be beneficial and often times, a circular boundary would match the AMPERE data better. Unfortunately, without better SuperDARN coverage at mid-latitudes and a way to assess the quality of convection maps, trust in the boundary is difficult to establish. This study has however also made clear that there are times when Λ_{Walach} and Λ_{Fogg} do not match, despite sufficient SuperDARN scatter to be confident of reliable boundary placement. As such, our physical understanding of these cases is lacking. A good example of this is the observation that the FAC systems sometimes contract much quicker than the

770 SuperDARN boundaries. As this happens on timescales that are several times longer than
 771 the Alfvén response times, we theorize that this is due to the inertia of the neutral at-
 772 mosphere affecting the ionosphere and AMPERE measures variations in the magnetic
 773 field, which do not always reflect changes in the ionosphere. This is a phenomenon that
 774 is poorly understood, especially since we observe this at the mid-latitudes, where Super-
 775 DARN observations have only been available since 2012. Furthermore, prior to Walach
 776 and Grocott (2019) and SuperDARN Data Analysis Working Group, Thomas, Ponomarenko,
 777 Billett, et al. (2018), all SuperDARN convection maps had a hard-coded 50° latitudi-
 778 nal limit for the convection boundary, which has previously hindered our ability to study
 779 expanded convection patterns in detail.

780 We have discussed challenges in comparing the AMPERE and SuperDARN datasets,
 781 which have highlighted that open questions remain regarding convection mapping. In
 782 summary, these open questions are:

- 783 • What makes a good quality map? Currently, there is no established criteria to eval-
 784 uate quality due to a lack of comparable datasets (see discussion in Walach et al.,
 785 2022a).
- 786 • What is the correct shape of the HMB? We have shown here that sometimes a cir-
 787 cular boundary may be more appropriate than what is currently used.
- 788 • How many vectors are enough to make a map and what should be used as a thresh-
 789 old for the HMB? We note here that Thomas and Shepherd (2018) for example
 790 used a more stringent criteria of 25 vectors with velocities greater than 150 m/s
 791 to determine the HMB location but this is not feasible for usual convection map-
 792 ping due to the vector coverage.
- 793 • Can we map convection in a coherent way which includes convection-related sub-
 794 auroral phenomena, such as SAPs?

795 Open Research

796 All SuperDARN and AMPERE data is openly available. Access to the SuperDARN
 797 database is available via the British Antarctic Survey and the University of Saskatchewan.
 798 The Radar Software Toolkit (RST) to process the SuperDARN data can be downloaded
 799 from <https://github.com/SuperDARN/rst> (SuperDARN Data Analysis Working Group,
 800 Thomas, Ponomarenko, Billett, et al., 2018). We thank the AMPERE team and the AM-
 801 PERE Science Center for providing the Iridium derived data products. All AMPERE
 802 data are available online (via <https://ampere.jhuapl.edu>). The SuperDARN convection
 803 maps used in this study, as well as the polar plots of SuperDARN and AMPERE and
 804 the Λ_{Fogg} and Λ_{Walach} values are available in Walach and Fogg (2024b). R_F boundaries
 805 are available online (from <https://doi.org/10.25392/leicester.data.11294861.v1>). We ac-
 806 knowledge use of NASA/GSFC’s Space Physics Data Facility’s CDAWeb service, and
 807 OMNI data. In the SI we show the solar wind data and geomagnetic indices at 1-minute
 808 resolution, which are extracted from the OMNI data (King & Papitashvili, 2005). The
 809 geomagnetic indices are also shown in Figures 1, 3 and 5. In the SI we also show Φ_D ,
 810 the dayside reconnection rate, which is derived from the OMNI data using the equation
 811 derived by Milan et al. (2012).

812 Acknowledgments

813 This work is dedicated to the memory of Kathryn McWilliams who suddenly passed away
 814 during the reviewing process of this manuscript. The authors acknowledge the use of Su-
 815 perDARN data. SuperDARN is a collection of radars funded by national scientific fund-
 816 ing agencies of Australia, Canada, China, France, Italy, Japan, Norway, South Africa,
 817 United Kingdom, and United States of America, and we thank the international PI team
 818 for providing the data. The authors acknowledge access to the SuperDARN database

819 via the Virginia Tech SuperDARN group and their website (<http://vt.superdarn.org/>).
 820 Other data mirrors are hosted by the British Antarctic Survey and the University of Saskatchewan.
 821 The Radar Software Toolkit (RST) to process the SuperDARN data can be downloaded
 822 from <https://github.com/SuperDARN/rst> (SuperDARN Data Analysis Working Group,
 823 Thomas, Ponomarenko, Billett, et al., 2018). MTW acknowledges the use of the Lan-
 824 caster University High-End Computing Cluster (HEC), which has greatly facilitated The
 825 SuperDARN data processing, and Mike Pacey's HEC support. The authors thank the
 826 SuperDARN PIs for their continued work in making SuperDARN data available and the
 827 SuperDARN Data Analysis Working Group in their ongoing efforts to improve the soft-
 828 ware quality and accessibility. Support for AMPERE has been provided under NSF award
 829 AGS-2002574. We thank the AMPERE team and the AMPERE Science Data Center
 830 for providing data products derived from the Iridium Communications constellation, en-
 831 abled by support from the National Science Foundation. We thank King, Papitashvili
 832 and NASA for the provision of the OMNI dataset through the CDAWeb service and ac-
 833 knowledge the use of this for the information shown in the SI.

834 MTW gratefully acknowledge funding through the UKRI STFC Ernest Ruther-
 835 ford fellowship (grant ST/X003663/1). MTW and AG gratefully acknowledge the fund-
 836 ing from the UKRI Natural Environment Funding Council (grants NE/T000937/1 and
 837 NE/P001556/1 and NE/V00283X/1). ARF was supported by an STFC studentship and
 838 Irish Research Council Government of Ireland Postdoctoral Fellowship (grant GOIPD/2022/782).
 839 ML and SEM acknowledge support from the UK Science and Technology Facilities Coun-
 840 cil (grant ST/W00089X/1). JCC acknowledges support from the UKRI STFC Ernest
 841 Rutherford Fellowship (grant ST/V004883/1). SKV and BJA were supported by NSF
 842 Award AGS-2002574.

843 For the purpose of open access, the authors have applied a Creative Commons At-
 844 tribution (CC BY) licence to any Author Accepted Manuscript version arising.

845 References

- 846 Anderson, B. J., Angappan, R., Barik, A., Vines, S. K., Stanley, S., Bernasconi,
 847 P. N., ... Barnes, R. J. (2021). Iridium communications satellite con-
 848 stellation data for study of earth's magnetic field. *Geochemistry, Geo-*
 849 *physics, Geosystems*, 22(8), e2020GC009515. Retrieved from [https://](https://agupubs.onlinelibrary.wiley.com/doi/abs/10.1029/2020GC009515)
 850 agupubs.onlinelibrary.wiley.com/doi/abs/10.1029/2020GC009515
 851 (e2020GC009515 2020GC009515) doi: [https://doi.org/10.1029/](https://doi.org/10.1029/2020GC009515)
 852 [2020GC009515](https://doi.org/10.1029/2020GC009515)
- 853 Anderson, B. J., Korth, H., Waters, C. L., Green, D. L., Merkin, V. G., Barnes,
 854 R. J., & Dyrud, L. P. (2014). Development of large-scale birkeland cur-
 855 rents determined from the active magnetosphere and planetary electrodynam-
 856 ics response experiment. *Geophysical Research Letters*, 41(9), 3017-3025.
 857 Retrieved from [https://agupubs.onlinelibrary.wiley.com/doi/abs/](https://agupubs.onlinelibrary.wiley.com/doi/abs/10.1002/2014GL059941)
 858 [10.1002/2014GL059941](https://doi.org/10.1002/2014GL059941) doi: <https://doi.org/10.1002/2014GL059941>
- 859 Anderson, B. J., Takahashi, K., & Toth, B. A. (2000). Sensing global birkeland
 860 currents with iridium® engineering magnetometer data. *Geophysical Research*
 861 *Letters*, 27(24), 4045-4048. Retrieved from [https://agupubs.onlinelibrary](https://agupubs.onlinelibrary.wiley.com/doi/abs/10.1029/2000GL000094)
 862 [.wiley.com/doi/abs/10.1029/2000GL000094](https://doi.org/10.1029/2000GL000094) doi: [https://doi.org/10.1029/](https://doi.org/10.1029/2000GL000094)
 863 [2000GL000094](https://doi.org/10.1029/2000GL000094)
- 864 Birkeland, K. R. (1908). *The Norwegian Aurora Polaris Expedition 1902-1903,*
 865 *vol. 1, first section, Part I, On the cause of magnetic storms and the origin of*
 866 *terrestrial magnetism*. Christiania: H. Aschehoug & Co.
- 867 Birkeland, K. R. (1913). *The Norwegian Aurora Polaris Expedition 1902-1903,*
 868 *vol. 1, second section, Part II, Polar magnetic phenomena and terrella experi-*
 869 *ments*. Christiania: H. Aschehoug & Co.
- 870 Bristow, W. A., & Jensen, P. (2007a). A superposed epoch study of SuperDARN

- 871 convection observations during substorms. *Journal of Geophysical Research:*
 872 *Space Physics*, 112(A6). doi: 10.1029/2006JA012049
- 873 Bristow, W. A., & Jensen, P. (2007b). A superposed epoch study of su-
 874 perdarn convection observations during substorms. *Journal of Geo-*
 875 *physical Research: Space Physics*, 112(A6). Retrieved from [https://](https://agupubs.onlinelibrary.wiley.com/doi/abs/10.1029/2006JA012049)
 876 agupubs.onlinelibrary.wiley.com/doi/abs/10.1029/2006JA012049 doi:
 877 <https://doi.org/10.1029/2006JA012049>
- 878 Bristow, W. A., Otto, A., & Lummerzheim, D. (2001). Substorm convection pat-
 879 terns observed by the super dual auroral radar network. *Journal of Geophysi-*
 880 *cal Research: Space Physics*, 106(A11), 24593-24609. Retrieved from [https://](https://agupubs.onlinelibrary.wiley.com/doi/abs/10.1029/2001JA000117)
 881 agupubs.onlinelibrary.wiley.com/doi/abs/10.1029/2001JA000117 doi:
 882 <https://doi.org/10.1029/2001JA000117>
- 883 Bristow, W. A., Sofko, G. J., Stenbaek-Nielsen, H. C., Wei, S., Lummerzheim, D.,
 884 & Otto, A. (2003). Detailed analysis of substorm observations using su-
 885 perdarn, uvi, ground-based magnetometers, and all-sky imagers. *Journal of*
 886 *Geophysical Research: Space Physics*, 108(A3). Retrieved from [https://](https://agupubs.onlinelibrary.wiley.com/doi/abs/10.1029/2002JA009242)
 887 agupubs.onlinelibrary.wiley.com/doi/abs/10.1029/2002JA009242 doi:
 888 <https://doi.org/10.1029/2002JA009242>
- 889 Carter, J., Milan, S., Coxon, J., Walach, M.-T., & Anderson, B. (2016). Average
 890 field-aligned current configuration parameterized by solar wind conditions.
 891 *Journal of Geophysical Research A: Space Physics*, 121(2), 1294–1307. doi:
 892 10.1002/2015JA021567
- 893 Chisham, G., Lester, M., Milan, S. E., Freeman, M. P., Bristow, W. a., Grocott, a.,
 894 ... Walker, a. D. M. (2007). A decade of the Super Dual Auroral Radar Net-
 895 work (SuperDARN): Scientific achievements, new techniques and future direc-
 896 tions. *Surveys in Geophysics*, 28(1), 33–109. doi: 10.1007/s10712-007-9017-8
- 897 Clausen, L. B. N., H. Baker, J. B., Ruohoniemi, J. M., Milan, S. E., Coxon, J. C.,
 898 Wing, S., ... Anderson, B. J. (2013). Temporal and spatial dynamics of the
 899 regions 1 and 2 Birkeland currents during substorms. *Journal of Geophysical*
 900 *Research: Space Physics*, 118(6), 3007–3016. doi: 10.1002/jgra.50288
- 901 Cowley, S. W. H. (2000). Magnetosphere-ionosphere interactions: A tutorial re-
 902 view. In *Magnetospheric current systems* (p. 91-106). American Geophysical
 903 Union (AGU). Retrieved from [https://agupubs.onlinelibrary.wiley.com/](https://agupubs.onlinelibrary.wiley.com/doi/abs/10.1029/GM118p0091)
 904 [doi/abs/10.1029/GM118p0091](https://agupubs.onlinelibrary.wiley.com/doi/abs/10.1029/GM118p0091) doi: <https://doi.org/10.1029/GM118p0091>
- 905 Cowley, S. W. H., & Lockwood, M. (1992). Excitation and decay of solar wind-
 906 driven flows in the magnetosphere-ionosphere system. *Annales geophysicae*, 10,
 907 103–115.
- 908 Coxon, J. C., Chisham, G., Freeman, M. P., Forsyth, C., Walach, M.-T., Murphy,
 909 K. R., ... Fogg, A. R. (2023). Extreme birkeland currents are more likely
 910 during geomagnetic storms on the dayside of the earth. *Journal of Geophysical*
 911 *Research: Space Physics*, 128(12), e2023JA031946. Retrieved from [https://](https://agupubs.onlinelibrary.wiley.com/doi/abs/10.1029/2023JA031946)
 912 agupubs.onlinelibrary.wiley.com/doi/abs/10.1029/2023JA031946
 913 (e2023JA031946 2023JA031946) doi: <https://doi.org/10.1029/2023JA031946>
- 914 Coxon, J. C., Milan, S. E., & Anderson, B. J. (2018). A review of birkeland cur-
 915 rent research using ampere. In *Electric currents in geospace and beyond*
 916 (p. 257-278). American Geophysical Union (AGU). Retrieved from [https://](https://agupubs.onlinelibrary.wiley.com/doi/abs/10.1002/9781119324522.ch16)
 917 agupubs.onlinelibrary.wiley.com/doi/abs/10.1002/9781119324522.ch16
 918 doi: <https://doi.org/10.1002/9781119324522.ch16>
- 919 Coxon, J. C., Milan, S. E., Clausen, L. B. N., Anderson, B. J., & Korth, H. (2014).
 920 A superposed epoch analysis of the regions 1 and 2 Birkeland currents ob-
 921 served by AMPERE during substorms. *Journal of Geophysical Research: Space*
 922 *Physics*, 119, 1–13. doi: 10.1002/2014JA020500
- 923 Coxon, J. C., Rae, I. J., Forsyth, C., Jackman, C. M., Fear, R. C., & Ander-
 924 son, B. J. (2017). Birkeland currents during substorms: Statistical
 925 evidence for intensification of regions 1 and 2 currents after onset and

- 926 a localized signature of auroral dimming. *Journal of Geophysical Re-*
 927 *search: Space Physics*, 122(6), 6455-6468. Retrieved from [https://](https://agupubs.onlinelibrary.wiley.com/doi/abs/10.1002/2017JA023967)
 928 agupubs.onlinelibrary.wiley.com/doi/abs/10.1002/2017JA023967 doi:
 929 <https://doi.org/10.1002/2017JA023967>
- 930 Coxon, J. C., Shore, R. M., Freeman, M. P., Fear, R. C., Browett, S. D., Smith,
 931 A. W., ... Anderson, B. J. (2019). Timescales of birkeland currents driven
 932 by the imf. *Geophysical Research Letters*, 46(14), 7893-7901. Retrieved
 933 from [https://agupubs.onlinelibrary.wiley.com/doi/abs/10.1029/](https://agupubs.onlinelibrary.wiley.com/doi/abs/10.1029/2018GL081658)
 934 [2018GL081658](https://agupubs.onlinelibrary.wiley.com/doi/abs/10.1029/2018GL081658) doi: <https://doi.org/10.1029/2018GL081658>
- 935 Davis, T. N., & Sugiura, M. (1966). Auroral electrojet activity index AE and its
 936 universal time variations. *Journal of Geophysical Research*, 71(3). doi: 10
 937 .1029/JZ071i003p00785
- 938 Dungey, J. W. (1961). Interplanetary Magnetic Field and the Auroral Zones. *Physi-*
 939 *cal Review Letters*, 6(2), 47-48. doi: 10.1103/PhysRevLett.6.47
- 940 Dungey, J. W. (1963). Interactions of solar plasma with the geomagnetic field. *Plan-*
 941 *etary and Space Science*, 10, 223-237. doi: 10.1016/0032-0633(63)90020-5
- 942 Elsdén, T., Yeoman, T. K., Wharton, S. J., Rae, I. J., Sandhu, J. K., Walach,
 943 M.-T., ... Wright, D. M. (2022). Modeling the varying location of field
 944 line resonances during geomagnetic storms. *Journal of Geophysical Re-*
 945 *search: Space Physics*, 127(1), e2021JA029804. Retrieved from [https://](https://agupubs.onlinelibrary.wiley.com/doi/abs/10.1029/2021JA029804)
 946 agupubs.onlinelibrary.wiley.com/doi/abs/10.1029/2021JA029804
 947 ([e2021JA029804](https://doi.org/10.1029/2021JA029804) [2021JA029804](https://doi.org/10.1029/2021JA029804)) doi: <https://doi.org/10.1029/2021JA029804>
- 948 Fogg, A. R. (2020, 2). SuperDARN Heppner-Maynard Boundaries. Retrieved from
 949 [https://leicester.figshare.com/articles/dataset/SuperDARN_Heppner](https://leicester.figshare.com/articles/dataset/SuperDARN_Heppner-Maynard_Boundaries/11854713)
 950 [-Maynard_Boundaries/11854713](https://leicester.figshare.com/articles/dataset/SuperDARN_Heppner-Maynard_Boundaries/11854713) doi: 10.25392/leicester.data.11854713.v1
- 951 Fogg, A. R., Lester, M., Yeoman, T. K., Burrell, A. G., Imber, S. M., Milan,
 952 S. E., ... Anderson, B. J. (2020). An improved estimation of Super-
 953 DARN Heppner-Maynard boundaries using AMPERE data. *Journal*
 954 *of Geophysical Research: Space Physics*, 125(5), e2019JA027218. Re-
 955 trieved from [https://agupubs.onlinelibrary.wiley.com/doi/abs/](https://agupubs.onlinelibrary.wiley.com/doi/abs/10.1029/2019JA027218)
 956 [10.1029/2019JA027218](https://agupubs.onlinelibrary.wiley.com/doi/abs/10.1029/2019JA027218) ([e2019JA027218](https://doi.org/10.1029/2019JA027218) [10.1029/2019JA027218](https://doi.org/10.1029/2019JA027218)) doi:
 957 <https://doi.org/10.1029/2019JA027218>
- 958 Foster, J. C., & Vo, H. B. (2002). Average characteristics and activity dependence
 959 of the subauroral polarization stream. *Journal of Geophysical Research: Space*
 960 *Physics*, 107. doi: 10.1029/2002JA009409
- 961 Gonzalez, W. D., Joselyn, J. A., Kamide, Y., Kroehl, H. W., Rostoker, G., Tsuru-
 962 tani, B. T., & Vasyliunas, V. M. (1994, April). What is a geomagnetic storm?
 963 *Journal of Geophysical Research*, 99, 5771-5792. doi: 10.1029/93JA02867
- 964 Greenwald, R. A., Baker, K. B., Dudeney, J. R., Pinnock, M., Jones, T. B., Thomas,
 965 E. C., ... Yamagishi, H. (1995). Darn/Superdarn; A Global View of the Dy-
 966 namics of High-Latitude Convection. *Space Science Reviews*, 71, 761-796. doi:
 967 10.1007/BF00751350
- 968 Heppner, J. P. (1972). Electric field variations during substorms: Ogo-6 mea-
 969 surements. *Planetary and Space Science*, 20(9), 1475-1498. Retrieved from
 970 <https://www.sciencedirect.com/science/article/pii/0032063372900529>
 971 doi: [https://doi.org/10.1016/0032-0633\(72\)90052-9](https://doi.org/10.1016/0032-0633(72)90052-9)
- 972 Heppner, J. P., & Maynard, N. C. (1987). Empirical high-latitude electric field
 973 models. *Journal of Geophysical Research*, 92(A5), 4467-4489. doi: 10.1029/
 974 JA092iA05p04467
- 975 Iijima, T., & Potemra, T. A. (1978). Large-scale characteristics of field-
 976 aligned currents associated with substorms. *Journal of Geophysical*
 977 *Research: Space Physics*, 83(A2), 599-615. Retrieved from [https://](https://agupubs.onlinelibrary.wiley.com/doi/abs/10.1029/JA083iA02p00599)
 978 agupubs.onlinelibrary.wiley.com/doi/abs/10.1029/JA083iA02p00599
 979 doi: <https://doi.org/10.1029/JA083iA02p00599>
- 980 Imber, S. M., Milan, S. E., & Lester, M. (2013a). The Heppner-Maynard Bound-

- ary measured by SuperDARN as a proxy for the latitude of the auroral oval.
Journal of Geophysical Research: Space Physics, 118(2), 685–697. doi:
 10.1029/2012JA018222
- Imber, S. M., Milan, S. E., & Lester, M. (2013b). Solar cycle variations in polar cap area measured by the superDARN radars. *Journal of Geophysical Research: Space Physics*, 118(10), 6188–6196. doi: 10.1002/jgra.50509
- Iyemori, T. (1990). Storm-time magnetospheric currents inferred from mid-latitude geomagnetic field variations. *Journal of geomagnetism and geoelectricity*, 42(11), 1249–1265. doi: 10.5636/jgg.42.1249
- King, J. H., & Papitashvili, N. E. (2005). Solar wind spatial scales in and comparisons of hourly Wind and ACE plasma and magnetic field data. *Journal of Geophysical Research: Space Physics*, 110, 1–9. doi: 10.1029/2004JA010649
- Kunduri, B. S. R., Baker, J. B. H., Ruohoniemi, J. M., Nishitani, N., Oksavik, K., Erickson, P. J., ... Miller, E. S. (2018, September). A new empirical model of the subauroral polarization stream. *J. Geophys. Res-Space Phys.*, 123(9), 7342–7357. doi: 10.1029/2018JA025690
- Lester, M. (2008). SuperDARN: An example of a network approach to geospace science in the twenty-first century. *Journal of Atmospheric and Solar-Terrestrial Physics*, 70(18), 2309–2323. doi: 10.1016/j.jastp.2008.08.003
- Lockwood, M. (1991). On flow reversal boundaries and transpolar voltage in average models of high-latitude convection. *Planetary and Space Science*, 39(3), 397–409. doi: 10.1016/0032-0633(91)90002-r
- Maimaiti, M., Baker, J. B. H., Ruohoniemi, J. M., & Kunduri, B. (2019). Morphology of nightside subauroral ionospheric convection: Monthly, seasonal, kp, and imf dependencies. *Journal of Geophysical Research: Space Physics*, 124(6), 4608–4626. Retrieved from <https://agupubs.onlinelibrary.wiley.com/doi/abs/10.1029/2018JA026268> doi: <https://doi.org/10.1029/2018JA026268>
- McWilliams, K. A., Yeoman, T. K., Sigwarth, J. B., Frank, L. A., & Brittnacher, M. (2001). The dayside ultraviolet aurora and convection responses to a southward turning of the interplanetary magnetic field. *Annales Geophysicae*, 19(7), 707–721. Retrieved from <https://angeo.copernicus.org/articles/19/707/2001/> doi: 10.5194/angeo-19-707-2001
- Milan, S. E. (2019, 12). AMPERE R1/R2 FAC radii. Retrieved from https://leicester.figshare.com/articles/dataset/AMPERE_R1_R2_FAC_radii/11294861 doi: 10.25392/leicester.data.11294861.v1
- Milan, S. E., Carter, J. A., Korth, H., & Anderson, B. J. (2015). Principal component analysis of birkeland currents determined by the active magnetosphere and planetary electrodynamics response experiment. *Journal of Geophysical Research: Space Physics*, 120(12), 10,415–10,424. Retrieved from <https://agupubs.onlinelibrary.wiley.com/doi/abs/10.1002/2015JA021680> doi: <https://doi.org/10.1002/2015JA021680>
- Milan, S. E., Clausen, L., Coxon, J., Carter, J., Walach, M.-T., Laundal, K., ... Anderson, B. J. (2017). Overview of solar wind-magnetosphere-ionosphere-atmosphere coupling and the generation of magnetospheric currents. *Space Science Reviews*.
- Milan, S. E., Gosling, J. S., & Hubert, B. (2012). Relationship between interplanetary parameters and the magnetopause reconnection rate quantified from observations of the expanding polar cap. *Journal of Geophysical Research*, 117(A3), A03226. doi: 10.1029/2011JA017082
- Milan, S. E., Sato, N., Ejiri, M., & Moen, J. (2001). Auroral forms and the field-aligned current structure associated with field line resonances. *Journal of Geophysical Research: Space Physics*, 106(A11), 25825–25833. Retrieved from <https://agupubs.onlinelibrary.wiley.com/doi/abs/10.1029/2001JA900077> doi: <https://doi.org/10.1029/2001JA900077>

- 1036 Nishitani, N., Ruohoniemi, J. M., Lester, M., Baker, J. B. H., Koustov, A. V., Shep-
 1037 herd, S. G., ... Kikuchi, T. (2019). Review of the accomplishments of mid-
 1038 latitude super dual auroral radar network (superdarn) hf radars. *Progress in*
 1039 *Earth and Planetary Science*, 6(1), 27. doi: 10.1186/s40645-019-0270-5
- 1040 Obayashi, T., & Nishida, A. (1968). Large-scale electric field in the magneto-
 1041 sphere. *Space Science Reviews*, 8(1), 3–31. Retrieved from [https://doi.org/](https://doi.org/10.1007/BF00362569)
 1042 [10.1007/BF00362569](https://doi.org/10.1007/BF00362569) doi: 10.1007/BF00362569
- 1043 Parker, E. N. (1996). The alternative paradigm for magnetospheric physics. *Journal*
 1044 *of Geophysical Research: Space Physics*, 101(A5), 10587-10625. Retrieved from
 1045 <https://agupubs.onlinelibrary.wiley.com/doi/abs/10.1029/95JA02866>
 1046 doi: <https://doi.org/10.1029/95JA02866>
- 1047 Parker, E. N. (1997). Reply [to “comment on “the alternative paradigm for
 1048 magnetospheric physics” by e. n. parker”]. *Journal of Geophysical Re-*
 1049 *search: Space Physics*, 102(A5), 9657-9658. Retrieved from [https://](https://agupubs.onlinelibrary.wiley.com/doi/abs/10.1029/97JA00347)
 1050 agupubs.onlinelibrary.wiley.com/doi/abs/10.1029/97JA00347 doi:
 1051 <https://doi.org/10.1029/97JA00347>
- 1052 Pierrard, V., Botek, E., Ripoll, J.-F., Thaller, S. A., Moldwin, M. B., Ruohoniemi,
 1053 M., & Reeves, G. (2021). Links of the plasmopause with other boundary lay-
 1054 ers of the magnetosphere: Ionospheric convection, radiation belt boundaries,
 1055 auroral oval. *Frontiers in Astronomy and Space Sciences*, 8. Retrieved from
 1056 <https://www.frontiersin.org/articles/10.3389/fspas.2021.728531>
 1057 doi: 10.3389/fspas.2021.728531
- 1058 Provan, G., Lester, M., Mende, S., & Milan, S. E. (2004). Statistical study of high-
 1059 latitude plasma flow during magnetospheric substorms. *Annales Geophysicae*,
 1060 22(10), 3607–3624.
- 1061 Rankin, R., Kabin, K., Lu, J. Y., Mann, I. R., Marchand, R., Rae, I. J., ... Dono-
 1062 van, E. F. (2005). Magnetospheric field-line resonances: Ground-based ob-
 1063 servations and modeling. *Journal of Geophysical Research: Space Physics*,
 1064 110(A10). Retrieved from [https://agupubs.onlinelibrary.wiley.com/doi/](https://agupubs.onlinelibrary.wiley.com/doi/abs/10.1029/2004JA010919)
 1065 [abs/10.1029/2004JA010919](https://doi.org/10.1029/2004JA010919) doi: <https://doi.org/10.1029/2004JA010919>
- 1066 Ruohoniemi, J. M., & Baker, K. B. (1998). Large-scale imaging of high-latitude con-
 1067 vection with Super Dual Auroral Radar Network HF radar observations. *Jour-*
 1068 *nal of Geophysical Research*, 103(A9), 20797. doi: 10.1029/98JA01288
- 1069 Sandhu, J. K., Rae, I. J., Staples, F. A., Hartley, D. P., Walach, M.-T., Elsdén, T.,
 1070 & Murphy, K. R. (2021). The roles of the magnetopause and plasmopause
 1071 in storm-time ulf wave power enhancements. *Journal of Geophysical Re-*
 1072 *search: Space Physics*, 126(7), e2021JA029337. Retrieved from [https://](https://agupubs.onlinelibrary.wiley.com/doi/abs/10.1029/2021JA029337)
 1073 agupubs.onlinelibrary.wiley.com/doi/abs/10.1029/2021JA029337
 1074 (e2021JA029337 2021JA029337) doi: <https://doi.org/10.1029/2021JA029337>
- 1075 Sandhu, J. K., Rae, I. J., & Walach, M.-T. (2021). Challenging the use of ring
 1076 current indices during geomagnetic storms. *Journal of Geophysical Re-*
 1077 *search: Space Physics*, 126(2), e2020JA028423. Retrieved from [https://](https://agupubs.onlinelibrary.wiley.com/doi/abs/10.1029/2020JA028423)
 1078 agupubs.onlinelibrary.wiley.com/doi/abs/10.1029/2020JA028423
 1079 (e2020JA028423 2020JA028423) doi: <https://doi.org/10.1029/2020JA028423>
- 1080 Sandhu, J. K., Rae, I. J., Wygant, J. R., Breneman, A. W., Tian, S., Watt, C. E. J.,
 1081 ... Walach, M.-T. (2021). Ulf wave driven radial diffusion during geomag-
 1082 netic storms: A statistical analysis of van allen probes observations. *Journal*
 1083 *of Geophysical Research: Space Physics*, 126(4), e2020JA029024. Retrieved
 1084 from [https://agupubs.onlinelibrary.wiley.com/doi/abs/10.1029/](https://agupubs.onlinelibrary.wiley.com/doi/abs/10.1029/2020JA029024)
 1085 [2020JA029024](https://doi.org/10.1029/2020JA029024) (e2020JA029024 2020JA029024) doi: [https://doi.org/10.1029/](https://doi.org/10.1029/2020JA029024)
 1086 [2020JA029024](https://doi.org/10.1029/2020JA029024)
- 1087 Sangha, H., Milan, S. E., Carter, J. A., Fogg, A. R., Anderson, B. J., Korth, H.,
 1088 & Paxton, L. J. (2020). Bifurcated region 2 field-aligned currents asso-
 1089 ciated with substorms. *Journal of Geophysical Research: Space Physics*,
 1090 125(1), e2019JA027041. Retrieved from <https://agupubs.onlinelibrary>

- 1091 .wiley.com/doi/abs/10.1029/2019JA027041 (e2019JA027041
 1092 10.1029/2019JA027041) doi: <https://doi.org/10.1029/2019JA027041>
- 1093 Shepherd, S. G. (2014). Altitude-adjusted corrected geomagnetic coordinates: Def-
 1094 inition and functional approximations. *Journal of Geophysical Research: Space*
 1095 *Physics*, 119(9), 7501-7521. doi: 10.1002/2014JA020264
- 1096 Shepherd, S. G., & Ruohoniemi, J. M. (2000). Electrostatic potential patterns in
 1097 the high-latitude ionosphere constrained by superdarn measurements. *Journal*
 1098 *of Geophysical Research: Space Physics*, 105(A10), 23005-23014. Retrieved
 1099 from [https://agupubs.onlinelibrary.wiley.com/doi/abs/10.1029/](https://agupubs.onlinelibrary.wiley.com/doi/abs/10.1029/2000JA000171)
 1100 [2000JA000171](https://doi.org/10.1029/2000JA000171) doi: 10.1029/2000JA000171
- 1101 Sofko, G. J., Greenwald, R., & Bristow, W. (1995). Direct determination of
 1102 large-scale magnetospheric field-aligned currents with superdarn. *Geo-*
 1103 *physical Research Letters*, 22(15), 2041-2044. Retrieved from [https://](https://agupubs.onlinelibrary.wiley.com/doi/abs/10.1029/95GL01317)
 1104 [agupubs.onlinelibrary.wiley.com/doi/abs/10.1029/95GL01317](https://doi.org/10.1029/95GL01317) doi:
 1105 <https://doi.org/10.1029/95GL01317>
- 1106 Stern, D. P. (1977). Large-scale electric fields in the earth's magnetosphere. *Re-*
 1107 *views of Geophysics*, 15(2), 156-194. Retrieved from [https://agupubs](https://agupubs.onlinelibrary.wiley.com/doi/abs/10.1029/RG015i002p00156)
 1108 [.onlinelibrary.wiley.com/doi/abs/10.1029/RG015i002p00156](https://doi.org/10.1029/RG015i002p00156) doi:
 1109 <https://doi.org/10.1029/RG015i002p00156>
- 1110 SuperDARN Data Analysis Working Group, Thomas, E. G., Ponomarenko, P. V.,
 1111 Billett, D. D., Bland, E. C., Burrell, A. G., ... Walach, M.-T. (2018,
 1112 August). *Superdarn radar software toolkit (rst) 4.2*. Retrieved from
 1113 <https://doi.org/10.5281/zenodo.1403226> doi: 10.5281/zenodo.1403226
- 1114 SuperDARN Data Analysis Working Group, Thomas, E. G., Ponomarenko,
 1115 P. V., Bland, E. C., Burrell, A. G., Kotyk, K., ... Walach, M.-T. (2018,
 1116 January). *Superdarn radar software toolkit (rst) 4.1*. Retrieved from
 1117 <https://doi.org/10.5281/zenodo.1143675> doi: 10.5281/zenodo.1143675
- 1118 Thomas, E. G., & Shepherd, S. G. (2018). Statistical patterns of ionospheric con-
 1119 vection derived from mid-latitude, high-latitude, and polar superdarn hf radar
 1120 observations. *Journal of Geophysical Research: Space Physics*, 123(4), 3196-
 1121 3216. Retrieved from [https://agupubs.onlinelibrary.wiley.com/doi/abs/](https://agupubs.onlinelibrary.wiley.com/doi/abs/10.1002/2018JA025280)
 1122 [10.1002/2018JA025280](https://doi.org/10.1002/2018JA025280) doi: <https://doi.org/10.1002/2018JA025280>
- 1123 Vasyliunas, V. M. (2001). Electric field and plasma flow: What drives what?
 1124 *Geophysical Research Letters*, 28(11), 2177-2180. Retrieved from [https://](https://agupubs.onlinelibrary.wiley.com/doi/abs/10.1029/2001GL013014)
 1125 [agupubs.onlinelibrary.wiley.com/doi/abs/10.1029/2001GL013014](https://doi.org/10.1029/2001GL013014) doi:
 1126 <https://doi.org/10.1029/2001GL013014>
- 1127 Vasyliunas, V. M. (2005). Relation between magnetic fields and electric cur-
 1128 rents in plasmas. *Annales Geophysicae*, 23(7), 2589-2597. Retrieved
 1129 from <https://angeo.copernicus.org/articles/23/2589/2005/> doi:
 1130 [10.5194/angeo-23-2589-2005](https://doi.org/10.5194/angeo-23-2589-2005)
- 1131 Walach, M.-T., & Fogg, A. (2024a, August). *Combined superdarn and ampere plots*.
 1132 Zenodo. Retrieved from <https://doi.org/10.5281/zenodo.13493214> doi:
 1133 [10.5281/zenodo.13493214](https://doi.org/10.5281/zenodo.13493214)
- 1134 Walach, M.-T., & Fogg, A. (2024b, August). *Lower latitude boundaries from AM-*
 1135 *PERE and SuperDARN*. Zenodo. Retrieved from [https://doi.org/10.5281/](https://doi.org/10.5281/zenodo.13495838)
 1136 [zenodo.13495838](https://doi.org/10.5281/zenodo.13495838) doi: 10.5281/zenodo.13495838
- 1137 Walach, M.-T., & Grocott, A. (2019). SuperDARN observations during geomagnetic
 1138 storms, geomagnetically active times, and enhanced solar wind driving. *Jour-*
 1139 *nal of Geophysical Research: Space Physics*, 124(7), 5828-5847. Retrieved
 1140 from [https://agupubs.onlinelibrary.wiley.com/doi/abs/10.1029/](https://agupubs.onlinelibrary.wiley.com/doi/abs/10.1029/2019JA026816)
 1141 [2019JA026816](https://doi.org/10.1029/2019JA026816) doi: 10.1029/2019JA026816
- 1142 Walach, M.-T., Grocott, A., & Milan, S. E. (2021). Average ionospheric electric field
 1143 morphologies during geomagnetic storm phases. *Journal of Geophysical Re-*
 1144 *search: Space Physics*, 126(4), e2020JA028512. Retrieved from [https://](https://agupubs.onlinelibrary.wiley.com/doi/abs/10.1029/2020JA028512)
 1145 [agupubs.onlinelibrary.wiley.com/doi/abs/10.1029/2020JA028512](https://doi.org/10.1029/2020JA028512)

- 1146 (e2020JA028512 2020JA028512) doi: <https://doi.org/10.1029/2020JA028512>
 1147 Walach, M.-T., Grocott, A., Staples, F., & Thomas, E. G. (2022a). Super dual
 1148 auroral radar network expansion and its influence on the derived ionospheric
 1149 convection pattern. *Journal of Geophysical Research: Space Physics*, *127*(2),
 1150 e2021JA029559. doi: 10.1029/2021JA029559
- 1151 Walach, M.-T., Grocott, A., Thomas, E. G., & Staples, F. (2022b). Dusk-dawn
 1152 asymmetries in superdarn convection maps. *Journal of Geophysical Re-*
 1153 *search: Space Physics*, *127*(12), e2022JA030906. Retrieved from [https://](https://agupubs.onlinelibrary.wiley.com/doi/abs/10.1029/2022JA030906)
 1154 agupubs.onlinelibrary.wiley.com/doi/abs/10.1029/2022JA030906
 1155 (e2022JA030906 2022JA030906) doi: <https://doi.org/10.1029/2022JA030906>
- 1156 Walach, M.-T., Milan, S. E., Yeoman, T. K., Hubert, B. A., & Hairston, M. R.
 1157 (2017a). Testing nowcasts of the ionospheric convection from the expand-
 1158 ing and contracting polar cap model. *Space Weather*, *15*(4), 623-636. doi:
 1159 10.1002/2017SW001615
- 1160 Waters, C. L., Anderson, B. J., Green, D. L., Korth, H., Barnes, R. J., & Van-
 1161 hamäki, H. (2020). Science data products for ampere. In M. W. Dunlop &
 1162 H. Lühr (Eds.), *Ionospheric multi-spacecraft analysis tools: Approaches for*
 1163 *deriving ionospheric parameters* (pp. 141-165). Cham: Springer International
 1164 Publishing. Retrieved from https://doi.org/10.1007/978-3-030-26732-2_7
 1165 doi: 10.1007/978-3-030-26732-2_7
- 1166 Waters, C. L., Anderson, B. J., & Liou, K. (2001). Estimation of global field aligned
 1167 currents using the iridium® system magnetometer data. *Geophysical Research*
 1168 *Letters*, *28*(11), 2165-2168. Retrieved from [https://agupubs.onlinelibrary](https://agupubs.onlinelibrary.wiley.com/doi/abs/10.1029/2000GL012725)
 1169 [.wiley.com/doi/abs/10.1029/2000GL012725](https://agupubs.onlinelibrary.wiley.com/doi/abs/10.1029/2000GL012725) doi: [https://doi.org/10.1029/](https://doi.org/10.1029/2000GL012725)
 1170 [2000GL012725](https://doi.org/10.1029/2000GL012725)
- 1171 Weygand, J. M., Ngwira, C. M., & Arritt, R. F. (2023). The equatorward boundary
 1172 of the auroral current system during magnetic storms. *Journal of Geophysical*
 1173 *Research: Space Physics*, *128*(6), e2023JA031510. Retrieved from [https://](https://agupubs.onlinelibrary.wiley.com/doi/abs/10.1029/2023JA031510)
 1174 agupubs.onlinelibrary.wiley.com/doi/abs/10.1029/2023JA031510
 1175 (e2023JA031510 2023JA031510) doi: <https://doi.org/10.1029/2023JA031510>
- 1176 Wharton, S. J., Rae, I. J., Sandhu, J. K., Walach, M.-T., Wright, D. M., & Yeoman,
 1177 T. K. (2020). The changing eigenfrequency continuum during geomag-
 1178 netic storms: Implications for plasma mass dynamics and ulf wave coupling.
 1179 *Journal of Geophysical Research: Space Physics*, *125*(6), e2019JA027648.
 1180 Retrieved from [https://agupubs.onlinelibrary.wiley.com/doi/abs/](https://agupubs.onlinelibrary.wiley.com/doi/abs/10.1029/2019JA027648)
 1181 [10.1029/2019JA027648](https://agupubs.onlinelibrary.wiley.com/doi/abs/10.1029/2019JA027648) (e2019JA027648 10.1029/2019JA027648) doi:
 1182 <https://doi.org/10.1029/2019JA027648>
- 1183 Wright, A. N., & Elsdén, T. (2020). Simulations of mhd wave propaga-
 1184 tion and coupling in a 3-d magnetosphere. *Journal of Geophysical Re-*
 1185 *search: Space Physics*, *125*(2), e2019JA027589. Retrieved from [https://](https://agupubs.onlinelibrary.wiley.com/doi/abs/10.1029/2019JA027589)
 1186 agupubs.onlinelibrary.wiley.com/doi/abs/10.1029/2019JA027589
 1187 (e2019JA027589 10.1029/2019JA027589) doi: [https://doi.org/10.1029/](https://doi.org/10.1029/2019JA027589)
 1188 [2019JA027589](https://doi.org/10.1029/2019JA027589)